CrossMark

ORIGINAL PAPER

Geochronological and mineral chemical constraints on the age and formation conditions of the leucogranite in the Mawat ophiolite, Northeastern of Iraq: insight to sync-subduction zone granite

Yousif O. Mohammad[1,2] · Jabbar H. Qaradaghi[1]

Abstract Daraban leucogranite occurs as cactus-like dykes hosted in serpentinized harzburgite in the mantle section of the Mawat ophiolite, Kurdistan region, northeastern Iraq. It has a primary mineral assemblage of quartz + orthoclase + albite + tourmaline + muscovite, with Mg-rich biotite, phlogopite, zircon, ilmenite–titanohematite exsolution, xenotime, and monazite as the most abundant accessory minerals. New laser ablation inductively coupled plasma mass spectrometry U–(Th)–Pb dating of zircon, monazite, and xenotime reveal a single episode of leucogranite magmatism in the Mawat ophiolite at 92.6 ± 1.2 Ma. These data indicate that the intrusion ages of leucogranite rocks postdate the 105 ± 5 Ma formation age of Mawat ophiolite obtained by K–Ar hornblende method. The leucogranite magma originated by anatexis of pelagic sediments during the late Cretaceous subduction in the Neo-Tethys Ocean, leading to the formation of the Mawat ophiolite as part of the main Zagros ophiolite belt in Iraq and Iran. Tourmaline and biotite from leucogranite dykes were examined regarding their microchemistry and formation environment. Electron microprobe studies show that the tourmalines form mainly dravite–schorl solid solutions with a tendency to schorl compositions. Biotites in the leucogranite have bimodal composition represents by phlogopite and Mg-

rich biotite. The tourmaline and biotite compositions, as well as field observations, appear to exclude a late-stage magmatic differentiation origin for the leucogranite. A probable source is S-type granitic magma rich in boron that resulted from the anatexis of silica-rich Ca-poor subduction wedge sediments like those of the Qulqula group. This intruded the ophiolites during the subduction stage. Calculated biotite and Fe–Ti oxide equilibria indicate that the parent magma formed along the subduction zone and solidified in the mantle wedge at a pressure 3.8–4.2 kbar, equivalent to 12.5–13.8 km depth.

Introduction

Syn-subduction zone granite (trondhjemites and leucogranite) in the mantle section of ophiolites is ubiquitous and minor, yet forms a genetically important component of the granitic constituent in ophiolite (Coleman and Peterman 1975; Koepke et al. 2007). These rocks are the products of plate convergence and may reflect end-member processes of the transition from oceanic ridge to subduction; they originate from different protoliths and thermal regimes (Aldiss 1978; Cox et al. 1999; Rollinson 2009; Mohammad et al. 2014; Shafaii Moghadam and Stern 2015). Mineralogical and geochronological studies of such granitic intrusions in ophiolites provide an important key for deciphering the geodynamic evolution of the ophiolite domains incorporated into the orogenic belts and closure of the Neo-Tethyan ocean. The tectonic history usually comprises an initial sea-floor spreading, followed by closure of the ocean by subduction and then obduction and emplacement of the ophiolite onto the continental margin and formation of a mountain belt (Hacker et al. 1996; Karaoğlan

Electronic supplementary material The online version of this article (doi:10.1007/s12517-016-2630-4) contains supplementary material, which is available to authorized users.

✉ Yousif O. Mohammad
yousif.mohammad@univsul.edu.iq

[1] Department of Geology, School of Science, Faculty of Science and Science Education, University of Sulaimani, Sulaymaniyah, Iraq

[2] Department of Earth Sciences, University of Gothenburg, P.O. Box 460, 40530 Gothenburg, Sweden

Springer

et al. 2012). Leucogranites in the Mawat ophiolite can record the most important magmato-tectonic events from subduction to the Eurasia–Arabia continental collision as it contains powerful datable phases like zircon-, monazite-, xenotime-, and potassium-bearing minerals.

The blocking temperatures of radioactive elements are diverse in different minerals and systems. In the case of the K–Ar system, the Ar blocking temperature is $510 \pm 25\ °C$ for hornblende and $300 \pm 50°C$ for biotite (Dodson and Mcclelland-Brown 1985). In the case of the U–Pb system, the blocking temperature is considered to be higher than 900 °C for zircon (Cherniak and Watson 2000).

A comprehensive knowledge of the age of variable datable phases of these rocks is critical to understand the geodynamic evolution of the Zagros belt and for testing and further formulating geodynamic models of the Zagros orogeny.

Tourmaline and biotite are ubiquitous ferromagnesian constituents in granite formed in different petrologic environments, due to their wide range of stability (Henry and Guidotti 1985; Abdel-Rahman 1994). The chemical compositions of the tourmaline and biotite reflect the bulk chemistry of the system in which they formed. Moreover they provide useful information about the physicochemical conditions of formation and are thus significant petrogenetic indicators (Wones and Eugster 1965; Speer 1984; Burkhard 1991, 1993; Dyar et al. 1998; Fuchs et al. 1998; London 1999; Torres-Ruiz et al. 2003).

A comprehensive knowledge of the age of variable datable phases of these rocks is critical to understanding the geodynamic evolution of the Zagros belt and further formulating geodynamic models of the Zagros orogeny. Therefore, in this work, we present geochronological data for the zircon, xenotime and monazite in the Daraban leucogranites that crop out in the central summit of the Mawat ophiolite. Moreover, we document by electron microprobe and scanning electron microscope the chemical composition of tourmaline and biotite to (1) assess the extent to which tourmaline and biotite chemistry reflects the bulk composition of the host rocks (2) understand the crystallization conditions of leucogranite in the ophiolite suite.

Geological overview

The northern part of Iraq, also called the Kurdistan region of Iraq, forms part of the major Zagros Orogenic Belt in Iraq and Iran that contains at least three confirmed Mesozoic Neo-Tethys ophiolites in the border region (Fig. 1a). They are from southeast to northwest, the Penjween, Mawat, and Hasanbag which are an integral part of the Imbricate Zone of the Iraqi Zagros Orogenic Belt.

The Zagros Orogenic Belt in Iraq comprises four parallel NW–SE-trending structural domains. These are the Sanandaj–Sirjan Zone, the Imbricate Zone, the Zagros High and Low Fold and Thrust Belts, and the Mesopotamian Foreland Basin. The Imbricate Zone is a NW–SE-trending narrow belt (15 km wide in the northwest and 25 km in the southeast). It consists of imbricated tectonic slices involving Qulqula radiolarite, Mesozoic ophiolites, Cretaceous–Tertiary sedimentary rocks and Walash volcanic rocks. The High Zagros Reverse Fault bounds the Imbricate Zone to the southwest (Berberian 1995). Vegetation and soil cover are minimal on the Mawat ophiolite, making the rocks almost completely accessible to observation. Field relations for the southern exposure from near Waraz village to the top of Root Mountain (Fig. 1b) show that the complex is an overturned continuous sequence with pillow basalt at the bottom (10–30 m thick), amphibolite gabbro in the middle (2,500–3,000 m thick), and ultramafic rocks at the top (200–400 m thick). Numerous pyroxenite dykes cutting the ultrmafic unit are also observed. A sheeted dike section is not present or missing in southern section of the Mawat ophiolite. Hornblende K–Ar ages of mafic plutonic rocks suggest that the ophiolite crust was generated at 105 ± 5 Ma (Aswad and Elias 1988). However the youngest felsic magmatic activity in the ophiolite was dated at 93.4 ± 5.0 Ma by minerals and bulk rock Rb–Sr mineral isochron (Azizi et al. 2013). Azizi et al. (2013) considered that 93.4 ± 5.0 Ma is the age of collision of the Arabian passive margin with the Biston-Avoraman block (BAB), but no geological and field evidence of presence of BAB indicated in the area (Baziany 2014). There is general agreement that the Mawat ophiolite represents a Mesozoic subduction type of ophiolite formed in a forearc shortly after initiation of subduction and it is geochemically correlated with the Oman and Troodos ophiolites (Aswad and Elias 1988; Ismail et al. 2010; Ali et al. 2013; Mohammad et al. 2014). Meanwhile Azizi et al. (2013) suggested a mantle plume origin for the Mawat ophiolite. This controversy is mainly due to an absent of up to date solid geological map of the area, as the area till now is politically unstable region and the only available geological mapping in the area is from the mid twentieth century. Moreover the main mafic–ultramafic rock units were not mapped accurately due to the allochthones nature of Mawat ophiolite by thrusting and difficulty in accessing the whole Mawat area due to random distribution of land mines during Iraq–Iran war.

There are numerous white-colored leucogranitic intrusions in the mantle section of the Mawat ophiolite. They consist of small (>20 m) bodies and smaller, 2 to 10 m-thick-branched dikes in the partly serpentinized harzburgites of the upper most mantle portion of the ophiolite (Fig. 2a, b, c). The Daraban leucogranite has geographical coordinate's longitude 45° 32′ 12″ east and latitude 35° 51′ 28″ north, 2,005 m above sea levels. In the field the leucogranite appear as cactus tree-like, typically having a single more-or-less massive trunk topped by several small branches.
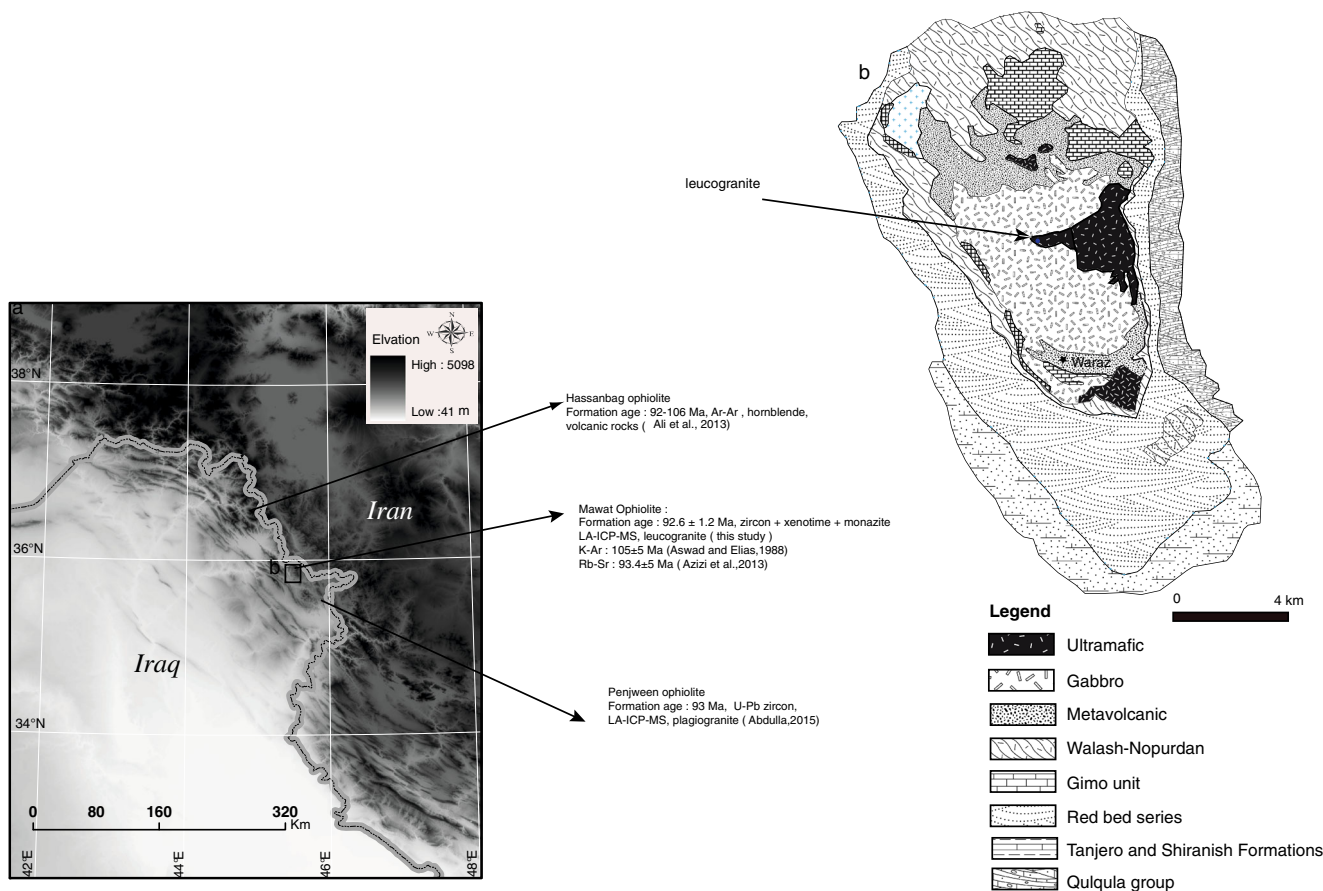
Fig. 1 **a** Digital elevation model of Iraq and adjacent regions based on Shuttle Radar Topography Mission (SRTM) data showing the locations of late cretaceous ophiolites in Iraq. **b** Geological map of the Mawat ophiolite complex (Al-Mehidi 1975)

These granitic intrusions at Daraban village are interpreted as magma resulting from anatexis of sedimentary crustal rocks based on whole rock geochemistry (Mohammad et al. 2014).

The leucogranite intrusions contain quartz, K-feldspar, plagioclase, muscovite, tourmaline, and biotite crystals that are mostly anhedral to subhedral, fine to medium grained. Muscovite shows slight post-crystallization plastic deformation. Monazite, xeotime and zircon are frequently observed and ilmenite–titanohematite exsolution intergrowths are the only opaque phase. In thin section tourmaline crystals show distinct zoning, frequently from a greenish blue core to a greenish crystal rim. The leucogranite contains ~75 wt% SiO_2 (Mohammad et al. 2014) and geochemically resemble subduction leucogranites from the northern Oman ophiolite (Cox et al. 1999) and continental collision zones like the Himalaya (Haase et al. 2015).

Biotite is the common accessory hydrous mafic mineral in the Daraban leucogranite dyke with modal proportion >1 %. It occurs as subhedral to anhedral grains that vary from 0.5 to 2 mm in diameter. However, it is also present in flake assemblages in the majority of rock samples, the textures are consistent with a primary magmatic origin. Flakes of biotite also occur as inclusions in tourmaline. Reddish brown-colored biotite from the marginal zones in leucogranite displays an interesting contrast of pleochroism. In the 20-cm-thick marginal zone, it shows light brown to brown pleochroic colors whereas in the inner zone, it is more reddish brown (Fig. 3a, b), suggesting higher total Fe and Ti contents. In backscattered electron images, no chemical alteration like chloritization has been observed in the biotite grains and along cleavage planes.

The investigated tourmalines in hand sample occur as black subhedral elongate grains and as skeletal crystals. The tourmalines have grain sizes ranging in length from <1 to 10 mm. Fine-grained brown or green tourmaline is optically and chemically homogenous whereas coarse-grained tourmaline displays concentric optical zoning that is distinguished into two broad zones of varying extent and shape (Fig. 3c, d). The cores are olive green and rims are brownish green. The color change from core to rim involves sharp optical discontinuities. Coarse-grained tourmaline with scarce inclusions of biotite is seen in secondary electron images (SEM). In general, tourmaline seems to have crystallized later than biotite; however, the local occurrence of biotite as inclusions in tourmaline shows some exceptions.
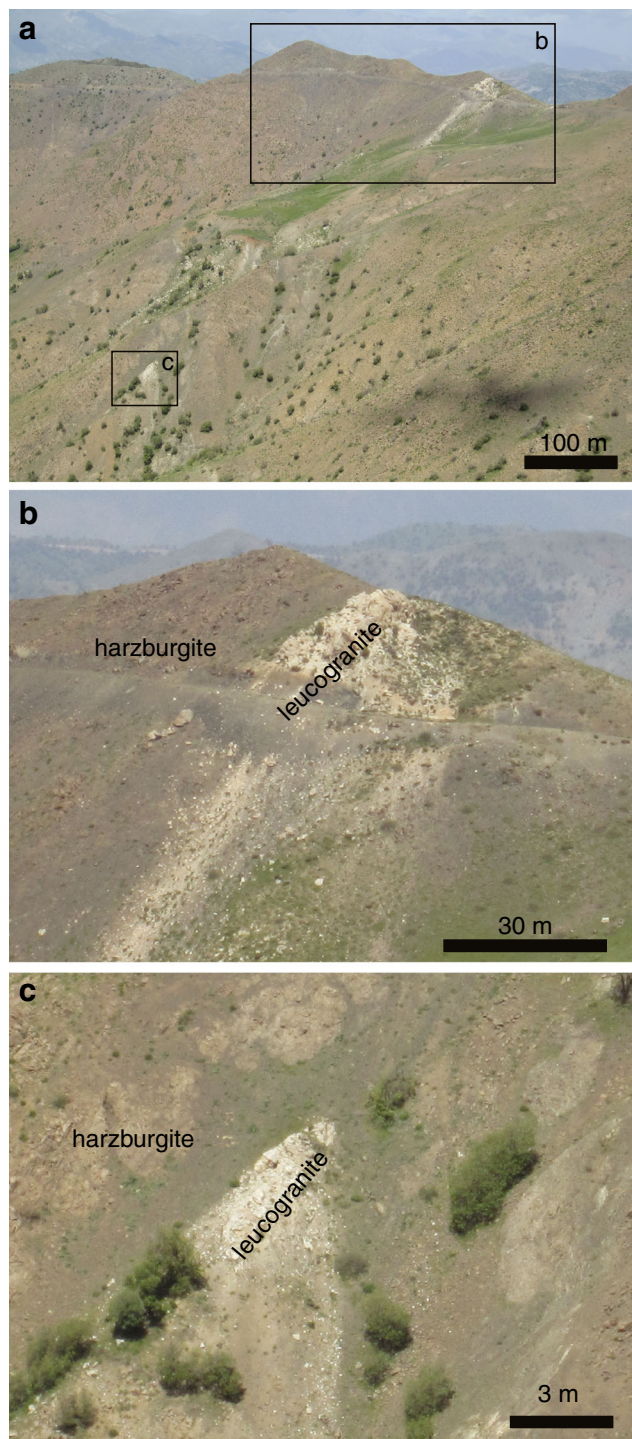
Fig. 2 **a**, **b**, and **c** Field photographs showing the field outcrops of leucogranite dikes hosted in harzburgite

Analytical methods

U–(Th)–Pb isotope analyses

Laser Ablation U–Pb dating was done at the University of Gothenburg as described by Cornell et al. (2013). A New Wave NWR213 laser ablation system was coupled to an

Agilent 7500a quadrupole ICP–MS. A 25-μm spot size was used for zircon and 5-μm for monazite and xenotime. The helium carrier gas was mixed with argon and nitrogen. Th and U concentrations and $^{206}Pb/^{204}Pb$ ratios were calculated from time–resolved raw counts, whereas $^{207}Pb/^{235}U$, $^{206}Pb/^{238}U$ and $^{208}Pb/^{232}Th$ ages (and their respective errors) were calculated from averaged ratios with an in-house Excel spreadsheet. The zircon standard GJ (Jackson et al. 2004) and monazite standard 44069 (Aleinikoff et al. 2006) were used as primary standards and to correct for fractionation. The overall accuracy for $^{207}Pb/^{235}U$, $^{206}Pb/^{238}U$, and $^{208}Pb/^{232}Th$ ages using this method is currently given as 1.5 % (Zirkler et al. 2012). Accurate $^{206}Pb/^{204}Pb$ ratios are not obtained due to mercury interference and cannot be used for common Pb correction, but rather serve as a qualitative estimate of common lead. During data collection for this study, concordia age results were obtained for several zircon and monazite standards, as given in (Supplementary 1).

The results are generally within the error of published ages. The LA–ICP-MS U–Pb data for zircon, monazite, and xenotime are given in Tables 1 and 2, respectively. U–Pb age calculations were made using the Isoplot 3.2 program of Ludwig (2003). Uncertainties of age calculations are all given at the 2σ level, ignoring decay constant errors. A few analysis points intersected inclusions, giving rise to high common lead and uneven data in time-resolved traces and these data were discarded.

Mineral chemistry

The Daraban leucogranite dyke we sampled appears relatively homogeneous at outcrop scale, although microscopic and geochemical studies show some slight changes in mineralogy particularly in the marginal zone with the host peridotite. Tourmaline and biotite were analyzed using a JEOL JAX850 hyperprobe at Geoanalytical laboratory, Washington State University, School of Earth and Environmental Sciences, Pullman USA, operating at 15.0 kV and 0.5 nA specimen current. Suitable synthetic and natural mineral standards were used. We also used a Hitachi S-400N scanning electron microscope at the Department of Earth Sciences at Gothenburg University, Sweden. The analytical conditions were: 20 kV, working distance 10-mm, specimen current 6 nA. Simple oxide and metal standards were used for calibration, linked to a cobalt reference standard and checked with Smithsonian mineral standards. Formulae calculations of mica were accomplished with the Mica$^+$ geological software (Yavuz 2003). Mica$^+$ uses the Dymek's (1983) normalization technique in calculating the ferric iron content of micas based on 22+ z cations. The structural formulae of tourmalines were calculated by the WinTcac software (Yavuz et al. 2014) on the basis of 31 oxygen anions. Ilmenite

Fig. 3 Photomicrographs in thin section of biotite and tourmaline in leucogranite dyke. **a** Dark reddish biotite in the inner zone specify: sample DL3, 1 m from contact. **b** Reddish brown color biotite from marginal zone, sample DL1C, 5 cm from contact. **c** Tourmaline showing olive-green core with brownish green rims, sample DL2, 50 cm from contact. **d** Coarse brownish green tourmaline, sample DL2
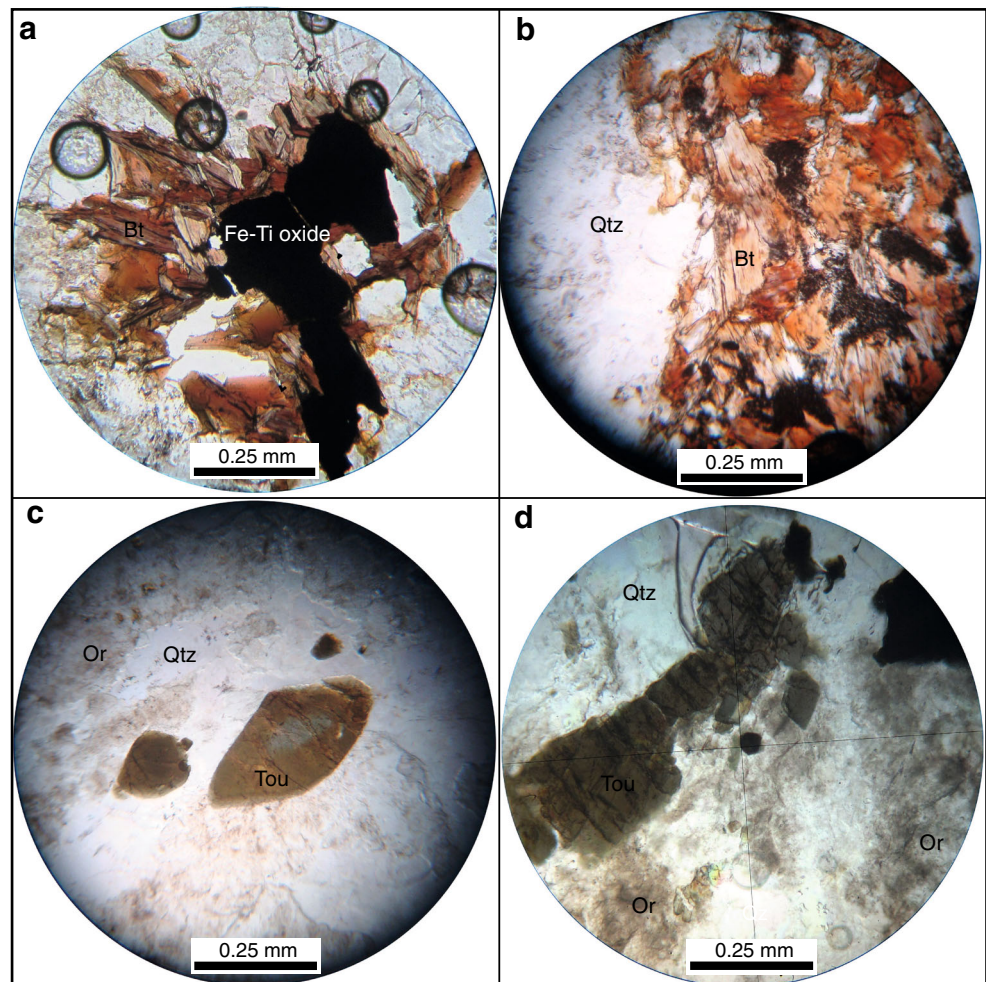
and titanohematite formulae are calculated based on 3 and 4 oxygens respectively. The electron microprobe micro-analysis (EPMA) results of tourmaline, biotite and Fe–Ti oxides are given in Tables 3, 4, and 5, respectively.

Results

Geochronology

The zircons from two equigranular Daraban leucogranite samples (DL3 and DL4) are euhedral to subhedral and are typically 50–150 μm long with length-to-width ratios ranging from ~1 to 3. In the CL images, most zircon grains show oscillatory zonation typical of magmatic zircon. All spots had very high uranium levels ranging from 4,000 to 14,000 ppm and relatively low Th concentrations and low Th/U ratios, suggesting that all the zircon belongs to the same magmatic population that grew in the parental magma of the dykes. Zircon in DL3 was concordant and

gave a U-Pb age of 92.5 ± 1.5 Ma on 11 points, with three omitted as shown in Fig. (4a).

Zircon in sample DL4 was concordant except for two points that had significant common lead and plot below concordia, as shown in Fig. (4b). Omitting one slightly older point, a concordia age of 92.9 ± 1.7 Ma was calculated for ten points. One grain of xenotime was found attached to a zircon in sample DL3 and was analyzed using the standard monazite calibration. One data point near the rim of the grain had significant common lead and plotted above concordia, but the other three gave a concordia age of 94.6 ± 2.2 Ma, as shown in Fig. (5a). The Th–Pb age on the same points is 91.6 ± 3.5 Ma. Several grains of monazite were found and three were analyzed in sample DL2. SEM examination of the monazite grains showed that grains 1 and 5 are cut by fractures that have much higher Th levels (Fig. 5b), whereas grain 3 is unaltered. The 18 data points show the influence of both common lead, giving high $^{207}Pb/^{206}Pb$ ratios and possible lead loss, giving younger U–Pb ages as shown in the Tera-Wasserburg plot (Fig 6a). It is thought that Th enrichment, lead loss and incorporation of common lead along fractures

Table 1 LA-ICP-MS U–Pb zircon data for Daraban leucogranite dyke samples DL3 and DL4

Spot	$\frac{207Pb}{206Pb}$	σ abs.	$\frac{207Pb}{235U}$	σ abs.	$\frac{206Pb}{238U}$	σ abs.	error correl.	$\frac{208Pb}{232U}$	σ abs.	$\frac{207Pb}{235U}$	±σ Ma	$\frac{206Pb}{238U}$	±σ Ma	$\frac{208Pb}{232Th}$	±σ Ma	U ppm	Th ppm	Th/U
DL3																		
14	0.0518	0.0010	0.0958	0.0024	0.0134	0.0002	0.62	0.00400	0.00020	92.9	2.2	86.0	1.6	80.7	4.1	9,475	762	0.08
16	0.0491	0.0012	0.0900	0.0030	0.0133	0.0003	0.69	0.00405	0.00043	87.5	2.8	85.0	2.1	81.6	8.6	8,817	339	0.04
26	0.0482	0.0026	0.0914	0.0051	0.0138	0.0007	0.53	0.00407	0.00032	88.8	4.7	88.1	4.7	82.1	6.5	10,312	369	0.04
31	0.0502	0.0042	0.0985	0.0089	0.0142	0.0012	0.56	0.00374	0.00051	95.4	8.3	91.1	7.9	75.4	10.2	6,158	470	0.08
32	0.0481	0.0011	0.0953	0.0029	0.0144	0.0003	0.64	0.00306	0.00023	92.5	2.7	92.1	2.1	61.7	4.7	6,638	351	0.05
40	0.0499	0.0011	0.0991	0.0031	0.0144	0.0004	0.70	0.00372	0.00020	95.9	2.8	92.2	2.3	75.0	4.0	7,424	562	0.08
42	0.0471	0.0014	0.0963	0.0036	0.0148	0.0005	0.64	0.00302	0.00026	93.4	3.3	94.9	3.0	60.9	5.3	7,051	362	0.05
43	0.0490	0.0011	0.1005	0.0031	0.0149	0.0004	0.67	0.00341	0.00018	97.3	2.9	95.2	2.4	68.8	3.7	11,655	959	0.08
52	0.0502	0.0010	0.1001	0.0027	0.0145	0.0003	0.67	0.00435	0.00024	96.9	2.5	92.6	1.8	87.7	4.9	11,914	783	0.07
53	0.0481	0.0012	0.0943	0.0029	0.0142	0.0004	0.65	0.00320	0.00016	91.5	2.7	91.1	2.3	64.5	3.3	9,986	622	0.06
65	0.0481	0.0011	0.0962	0.0030	0.0145	0.0004	0.66	0.00377	0.00021	93.3	2.7	92.9	2.3	76.1	4.2	8,241	454	0.06
70	0.0495	0.0012	0.0960	0.0030	0.0141	0.0003	0.64	0.00428	0.00029	93.1	2.8	90.1	2.1	86.3	5.9	6,503	325	0.05
75a	0.0479	0.0010	0.1002	0.0027	0.0152	0.0003	0.64	0.00377	0.00028	97.0	2.5	97.1	1.9	75.9	5.7	7,462	283	0.04
75b	0.0511	0.0011	0.1055	0.0029	0.0150	0.0003	0.63	0.00457	0.00029	101.9	2.7	95.8	1.9	92.1	5.7	7,494	495	0.07
DL4																		
14	0.0462	0.0014	0.0914	0.0033	0.0144	0.0005	0.60	0.00240	0.00035	88.8	3.1	91.9	2.9	48.4	7.0	12,661	1478	0.12
16	0.0460	0.0011	0.0928	0.0031	0.0146	0.0004	0.69	0.00244	0.00036	90.1	2.9	93.6	2.7	49.3	7.3	11,235	418	0.04
19a	0.0495	0.0022	0.1051	0.0057	0.0154	0.0008	0.67	0.00621	0.00104	101.5	5.3	98.5	5.2	125.1	20.9	4,401	94	0.02
19b	0.0487	0.0013	0.0957	0.0031	0.0142	0.0004	0.63	0.00259	0.00041	92.8	2.9	91.2	2.5	52.3	8.3	8,261	607	0.07
24	0.0465	0.0009	0.0947	0.0027	0.0148	0.0004	0.72	0.00262	0.00037	91.8	2.5	94.4	2.3	52.9	7.5	11,747	728	0.06
25	0.0507	0.0019	0.1079	0.0049	0.0154	0.0007	0.65	0.00620	0.00100	104.1	4.5	98.7	4.2	124.8	20.0	4,907	135	0.03
33	0.0473	0.0010	0.0932	0.0027	0.0143	0.0003	0.71	0.00261	0.00037	90.5	2.5	91.6	2.2	52.7	7.5	10,189	742	0.07
37	0.0612	0.0014	0.1060	0.0036	0.0126	0.0004	0.74	0.00473	0.00069	102.3	3.3	80.5	2.2	95.3	13.9	6,398	516	0.08
41	0.0535	0.0014	0.0933	0.0031	0.0126	0.0004	0.68	0.00262	0.00040	90.6	2.9	80.9	2.5	52.9	8.0	11,501	1,535	0.13
51a	0.0475	0.0010	0.0993	0.0031	0.0152	0.0004	0.72	0.00273	0.00039	96.2	2.9	97.1	2.5	55.0	7.9	14,046	1,657	0.12
51b	0.0470	0.0011	0.0955	0.0030	0.0147	0.0004	0.68	0.00278	0.00041	92.6	2.8	94.3	2.6	56.1	8.2	23,817	2,306	0.10
52	0.0501	0.0015	0.1005	0.0039	0.0146	0.0005	0.66	0.00378	0.00063	97.2	3.6	93.1	3.1	76.2	12.6	7,357	382	0.05
70	0.0462	0.0017	0.0893	0.0041	0.0140	0.0006	0.64	0.00218	0.00034	86.9	3.8	89.7	3.8	44.0	6.8	11,219	2,145	0.19

Calculated ages, Ma

Table 2 LA-ICP-MS U–Pb xenotime and monazite data for Daraban leucogranite dyke samples DL3 and DL4

Spot	$\frac{207Pb}{206Pb}$	σ abs.	$\frac{207Pb}{235U}$	σ abs.	$\frac{206Pb}{238U}$	σ abs.	error correl.	$\frac{208Pb}{232U}$	σ abs.	$\frac{207Pb}{235U}$	±σ Ma	$\frac{206Pb}{238U}$	±σ Ma	$\frac{208Pb}{232Th}$	±σ Ma	U ppm	Th ppm	Th/U
DL3 xenotime																		
66.1	0.0484	0.0015	0.0976	0.0029	0.0146	0.0003	0.35	0.00444	0.00015	94.6	2.7	93.5	2.1	89.6	3.0	17,969	14,935	0.83
66.2	0.0811	0.0031	0.1771	0.0069	0.0158	0.0004	0.31	0.00658	0.00017	165.6	6.0	101.3	2.3	132.5	3.5	18,820	15,495	0.82
66.3	0.0498	0.0016	0.0976	0.0030	0.0142	0.0003	0.32	0.00432	0.00017	94.6	2.8	91.1	2.1	87.0	3.4	17,424	13,562	0.78
66.4	0.0502	0.0015	0.1041	0.0029	0.0151	0.0003	0.30	0.00479	0.00014	100.6	2.7	96.3	2.0	96.6	2.8	14,277	8,745	0.61
DL4 monazite																		
1.1	0.0634	0.0023	0.0935	0.0050	0.0107	0.0005	0.75	0.00372	0.00014	90.7	4.6	68.6	3.2	75.0	2.9	6,805	92,526	13.60
1.2	0.0516	0.0020	0.0870	0.0039	0.0122	0.0004	0.55	0.00380	0.00014	84.7	3.7	78.4	2.7	76.6	2.8	5,160	88,455	17.14
1.3	0.0528	0.0017	0.0997	0.0037	0.0137	0.0003	0.52	0.00413	0.00011	96.5	3.4	87.7	2.1	83.3	2.3	5,221	77,758	14.89
1.4	0.0507	0.0019	0.0902	0.0038	0.0129	0.0004	0.51	0.00411	0.00013	87.7	3.5	82.6	2.4	82.9	2.6	4,468	74,909	16.76
1.5	0.0593	0.0024	0.1114	0.0054	0.0136	0.0005	0.57	0.00417	0.00016	107.3	4.9	87.2	3.1	84.0	3.3	6,063	83,541	13.78
1.6	0.0510	0.0014	0.0959	0.0034	0.0136	0.0005	0.69	0.00423	0.00022	92.9	3.1	87.2	3.0	85.3	4.4	14,952	67,353	4.50
3.1	0.0475	0.0018	0.0966	0.0037	0.0147	0.0004	0.39	0.00464	0.00017	93.7	3.4	94.3	2.7	93.5	3.4	8,095	83,971	10.37
3.2	0.0478	0.0018	0.0953	0.0035	0.0145	0.0004	0.37	0.00453	0.00017	92.4	3.3	92.5	2.7	91.3	3.3	8,072	85,767	10.62
3.3	0.0489	0.0019	0.0974	0.0039	0.0145	0.0005	0.41	0.00436	0.00010	94.4	3.6	92.5	3.0	87.8	2.0	9,688	105,825	10.92
3.4	0.0477	0.0011	0.0966	0.0021	0.0147	0.0002	0.21	0.00455	0.00005	93.6	2.0	93.9	1.4	91.7	1.1	7,608	66,801	8.78
3.5	0.0502	0.0014	0.0958	0.0033	0.0138	0.0004	0.64	0.00431	0.00016	92.9	3.0	88.6	2.6	86.9	3.2	10,476	83,543	7.97
3.6	0.0481	0.0020	0.0938	0.0043	0.0142	0.0006	0.55	0.00449	0.00019	91.1	4.0	90.6	3.6	90.5	3.9	6,721	117,203	17.44
5.1	0.4191	0.0300	1.0174	0.1186	0.0176	0.0020	0.81	0.00386	0.00017	712.6	61.5	112.5	12.8	77.9	3.3	4,964	127,647	25.72
5.2	0.0481	0.0020	0.0926	0.0043	0.0140	0.0006	0.57	0.00442	0.00023	89.9	4.0	89.4	3.8	89.1	4.6	4,152	67,441	16.24
5.3	0.3091	0.0106	0.8231	0.0345	0.0193	0.0007	0.63	0.00385	0.00015	609.8	19.4	123.3	4.5	77.7	2.9	4,067	100,784	24.78
5.4	0.1791	0.0141	0.4024	0.0322	0.0163	0.0007	0.32	0.00440	0.00024	343.4	23.6	104.2	4.7	88.8	4.8	6,291	99,003	15.74
5.5	0.0555	0.0029	0.1053	0.0057	0.0138	0.0007	0.54	0.00411	0.00017	101.6	5.3	88.1	4.6	82.8	3.4	4,403	10,2404	23.26
5.6	0.0530	0.0012	0.0944	0.0029	0.0129	0.0003	0.68	0.00397	0.00015	91.6	2.7	82.7	2.2	80.1	2.9	6,936	99,678	14.37

Calculated ages, Ma

Table 3 Representative microanalyses of the tourmaline from Daraban leucogranite dyke

Sample no.	DL2				DL2								DL3			DL3		
Oxide (wt%)	T-1	T-2	T-3	T-4	T-5	T-6	T-7	T-8	T-9	T-10	T-11	T-12	T-13	T-14	T-15	T-16	T-17	T-18
SiO_2	36.22	35.44	35.77	35.07	35.80	35.94	36.22	36.12	35.13	37.17	35.31	34.96	35.52	34.51	35.21	35.32	35.56	35.67
TiO_2	1.12	0.91	0.95	0.97	0.98	0.83	0.81	0.91	0.96	1.01	1.11	0.89	0.88	1.11	2.11	1.01	1.40	1.30
Al_2O_3	33.13	34.18	33.43	33.40	33.06	34.75	32.73	33.94	33.20	33.67	33.02	32.77	32.98	33.93	33.51	33.82	33.91	33.31
FeO	9.91	10.53	10.64	10.75	10.54	10.19	10.09	10.45	10.08	6.44	10.40	9.51	10.25	10.39	10.37	9.85	10.40	11.15
MnO	0.08	0.08	0.08	0.09	0.07	0.08	0.07	0.08	0.07	0.04	0.09	0.08	0.09	0.07	0.08	0.08	0.08	0.07
MgO	4.34	4.01	3.90	3.94	4.13	3.72	3.73	3.96	4.44	6.70	3.89	4.40	3.94	3.96	4.15	4.61	4.48	4.40
CaO	0.23	0.21	0.25	0.25	0.24	0.10	0.12	0.13	0.25	0.27	0.22	0.23	0.22	0.22	0.27	0.23	0.22	0.23
Na_2O	2.41	2.69	2.66	2.71	2.71	2.29	2.25	2.47	2.69	2.65	2.85	2.87	2.84	2.67	2.92	2.83	2.93	2.97
H_2O^*	3.35	3.46	3.41	3.43	3.43	3.33	3.23	3.38	3.43	3.48	3.42	3.41	3.41	3.42	3.49	3.50	3.54	3.56
B_2O_3	7.45	7.34	7.14	7.02	7.34	6.80	7.27	7.18	7.21	8.00	5.81	7.31	6.52	6.38	5.20	5.77	4.92	5.60
Total	98.22	98.84	98.23	97.63	98.30	98.00	96.51	98.61	97.46	99.42	96.11	96.43	96.57	96.65	97.30	97.01	97.44	98.26
Si	5.91	5.78	5.85	5.79	5.87	5.83	6.00	5.87	5.80	5.93	5.84	5.84	5.88	5.71	5.72	5.77	5.74	5.78
Ti	0.14	0.11	0.12	0.12	0.12	0.10	0.10	0.11	0.12	0.12	0.14	0.11	0.10	0.14	0.26	0.12	0.17	0.16
Al	6.37	6.57	6.45	6.50	6.39	6.65	6.39	6.50	6.46	6.33	6.43	6.45	6.43	6.61	6.41	6.51	6.46	6.36
Fe^{+2}	1.35	1.44	1.46	1.48	1.45	1.38	1.40	1.42	1.39	0.86	1.44	1.33	1.42	1.44	1.41	1.35	1.41	1.51
Mn	0.01	0.01	0.01	0.01	0.01	0.01	0.01	0.01	0.01	0.01	0.01	0.01	0.01	0.01	0.01	0.01	0.01	0.01
Mg	1.06	0.97	0.95	0.97	1.01	0.90	0.92	0.96	1.09	1.59	0.96	1.10	0.97	0.98	1.01	1.12	1.08	1.06
Ca	0.04	0.04	0.04	0.04	0.04	0.02	0.02	0.02	0.04	0.05	0.04	0.04	0.04	0.04	0.05	0.04	0.04	0.04
Na	0.76	0.85	0.84	0.87	0.86	0.72	0.72	0.78	0.86	0.82	0.91	0.93	0.91	0.86	0.92	0.90	0.92	0.93
B	3.00	3.00	3.00	3.00	3.00	3.00	3.00	3.00	3.00	3.00	3.00	3.00	3.00	3.00	3.00	3.00	3.00	3.00
X-vacancy	0.20	0.11	0.11	0.09	0.10	0.26	0.26	0.20	0.10	0.14	0.05	0.03	0.05	0.11	0.03	0.06	0.04	0.03
Fe#	0.56	0.60	0.61	0.61	0.59	0.61	0.60	0.60	0.56	0.35	0.60	0.55	0.59	0.60	0.58	0.55	0.57	0.59
Na/(Na+Ca)	0.95	0.96	0.95	0.95	0.95	0.98	0.97	0.97	0.95	0.95	0.96	0.96	0.96	0.96	0.95	0.96	0.96	0.96

H_2O^* calculated based on Win Tcac (Yavuz et al. 2014)

Table 4 Representative microanalyses of the biotite from Daraban leucogranite dyke

	Marginal zone										Inner zone									
	Phologopite (Fox-red colored)										Mg–biotite (Reddish brown colored)									
	DL1					DL10					DL3				DL5				DL7	
Sample no.	Ph-1	Ph-2	Ph-3	Ph-4	Ph-5	Ph-6	Ph-7	Ph-8	Ph-9	Ph-10	Mgb-1	Mgb-2	Mgb-3	Mgb-4	Mgb-5	Mgb-6	Mgb-7	Mgb-8	Mgb-9	Mgb-10
Oxides wt%																				
SiO_2	38.83	37.73	37.99	37.9	38.68	38.29	38.05	37.56	37.83	37.86	35.37	35.34	35.3	35.5	35.44	36.2	35.81	35.71	35.9	36.01
TiO_2	1.24	1.2	1.27	1.21	1.26	0.83	0.92	1.01	0.07	0.78	1.97	2.39	2.19	2.2	2.12	2.08	1.91	2.2	2.09	2.04
Al_2O_3	19.21	20.78	20.12	20.32	20.16	20.93	20.46	20.66	20.34	19.8	20.84	20.85	20.4	20.57	19.72	19.63	20.86	20.09	20.52	20.35
FeO	8.97	9.02	9.09	8.85	8.52	8.39	8.57	8.49	8.51	8.55	16.39	16.75	16.85	17.07	16.96	16.66	16.44	16.13	16.22	16.12
MnO	0.06	0.1	0.09	0.04	0.08	0.06	0.09	0.11	0.08	0.07	0.41	0.39	0.41	0.43	0.45	0.4	0.37	0.41	0.35	0.46
MgO	18.43	17.77	17.8	17.65	17.32	17.38	17.45	17.21	17.19	17.94	11.25	11.17	11.49	11.23	11.68	11.64	11.37	11.83	11.5	11.46
CaO	0.49	0.03	0.01	0.04	0.07	0.29	0.19	0.19	0.15	0.09	0.04	0.01	0.03	0.02	0.04	0.03	0.02	0.01	0.06	0.07
Na_2O	0.14	0.14	0.06	0.1	0.13	0.18	0.13	0.06	0.12	0.16	0.14	0.11	0.11	0.08	0.08	0.1	0.08	0.16	0.11	0.15
K_2O	8.92	10.12	10.09	10.02	9.7	9.12	9.39	10.17	9.71	9.9	9.86	10.03	9.82	10.04	9.64	9.8	9.9	9.69	9.46	10.21
Si	2.758	2.682	2.71	2.71	2.757	2.733	2.731	2.707	2.728	2.732	2.632	2.615	2.625	2.629	2.649	2.686	2.647	2.653	2.66	2.663
Al^{IV}	1.242	1.318	1.29	1.29	1.243	1.267	1.269	1.293	1.272	1.268	1.368	1.385	1.375	1.371	1.351	1.314	1.353	1.347	1.34	1.337
Al^{VI}	0.366	0.423	0.402	0.423	0.452	0.494	0.463	0.462	0.458	0.417	0.459	0.434	0.413	0.424	0.386	0.403	0.465	0.412	0.453	0.437
Ti	0.066	0.064	0.068	0.065	0.068	0.045	0.05	0.055	0.058	0.042	0.11	0.133	0.122	0.123	0.119	0.116	0.106	0.123	0.116	0.113
Fe^{+3}	0.04	0.07	0.061	0.101	0.18	0.19	0.152	0.181	0.179	0.145	0.08	0.02	0.015	0.023	0.042	0.054	0.091	0.012	0.05	0.143
Fe^{+2}	0.493	0.466	0.481	0.428	0.328	0.311	0.362	0.33	0.334	0.371	0.94	1.016	1.033	1.034	1.018	0.98	0.926	0.99	0.956	0.854
Mn	0.004	0.006	0.005	0.002	0.005	0.004	0.005	0.007	0.005	0.004	0.026	0.024	0.026	0.027	0.028	0.025	0.023	0.026	0.022	0.029
Mg	1.951	1.883	1.893	1.881	1.841	1.849	1.867	1.849	1.848	1.93	1.248	1.232	1.274	1.24	1.301	1.288	1.253	1.31	1.27	1.263
Ca	0.037	0.002	0.001	0.003	0.005	0.022	0.015	0.004	0.012	0.007	0.003	0.001	0.002	0.002	0.003	0.002	0.002	0.001	0.005	0.006
Na	0.019	0.019	0.008	0.014	0.018	0.025	0.018	0.008	0.017	0.022	0.02	0.016	0.016	0.016	0.012	0.014	0.011	0.023	0.016	0.022
K	0.808	0.918	0.918	0.914	0.882	0.83	0.86	0.935	0.893	0.912	0.936	0.947	0.932	0.948	0.919	0.928	0.934	0.918	0.894	0.963
Mg#	0.786	0.778	0.777	0.78	0.784	0.787	0.784	0.783	0.783	0.789	0.55	0.543	0.549	0.54	0.551	0.555	0.552	0.567	0.558	0.558
Fe/(Fe+Mg)	0.214	0.222	0.223	0.22	0.216	0.213	0.216	0.217	0.217	0.211	0.45	0.457	0.451	0.46	0.449	0.445	0.448	0.448	0.442	0.441
$Fe^{+2}/Fe^{+2}+Fe^{+3}$	0.925	0.869	0.887	0.809	0.646	0.621	0.704	0.646	0.65	0.719	0.921	0.981	0.986	0.978	0.96	0.947	0.911	0.988	0.951	0.857
$Fe^{+2}/Mg+Fe^{+2}$	0.202	0.198	0.203	0.185	0.151	0.144	0.163	0.152	0.153	0.161	0.43	0.452	0.448	0.455	0.439	0.432	0.425	0.43	0.429	0.403
T, °C	1,104.98	1,096.31	1,095.07	1,098.83	1,102.78	1,106.68	1,103.11	1,102.19	1,101.46	1,109.34	909.70	905.54	908.75	903.60	910.18	912.28	910.80	919.46	914.44	914.83
Log fO_2	−10.52	−10.38	−10.36	−10.42	−10.48	−10.54	−10.49	−10.47	−10.46	−10.58	−12.29	−13.20	−13.20	−13.20	−12.29	−12.30	−12.29	−12.31	−12.30	−12.30
^{T}Al	3.216	3.482	3.384	3.426	3.39	3.522	3.464	3.51	3.46	3.37	3.654	3.638	3.576	3.59	3.474	3.434	3.636	3.518	3.586	3.548
P Kbar	3.2	4.02	3.72	3.8	3.7	4.1	3.9	4.1	3.9	3.6	4.5	4.4	4.3	4.3	3.9	3.8	4.4	4.1	4.3	4.2
Depth in km	10.56	13.266	12.276	12.54	12.21	13.53	12.87	13.53	12.87	11.88	14.85	14.52	14.19	14.19	12.87	12.54	14.52	13.53	14.19	13.86

^{T} Al based on 22 oxygen

Table 5 Representative microanalyses of the Fe–Ti oxides from Daraban leucogranite dyke.

Fe–Ti oxide

Sample no.	DL3		DL3		DL5		DL5		DL5		
Oxides wt%	Tit-2	Il-2	Tit-3	Il-3	Tit-5	Il-5	Tit-6	Il-6	Tit-9	Il-9	Ilmo
TiO_2	19.50	47.66	19.33	48.22	19.42	48.53	18.91	48.24	18.81	47.65	33.73
Al_2O_3	0.00	0.40	0.19	0.01	0.27	0.05	0.26	0.09	0.19	0.13	0.13
FeO	80.35	50.55	80.04	51.06	79.73	50.45	80.34	50.47	80.82	50.95	65.00
MnO	0.00	1.18	0.00	0.61	0.00	0.86	0.14	1.02	0.05	1.09	0.45
MgO	0.20	0.23	0.41	0.09	0.38	0.12	0.25	0.18	0.13	0.18	0.28
Total	100.04	100.02	99.96	100.00	99.80	100.00	99.90	100.00	100.00	100.00	99.90
Ti	0.55	0.90	0.53	0.91	0.53	0.92	0.52	0.91	0.52	0.90	0.94
Al	0.00	0.01	0.01	0.00	0.01	0.00	0.01	0.00	0.01	0.00	0.01
Fe^{+3}	0.89	0.19	0.93	0.18	0.92	0.17	0.95	0.18	0.96	0.20	0.11
Fe^{+2}	1.54	0.86	1.51	0.89	1.51	0.89	1.50	0.88	1.51	0.87	1.92
Mn	0.00	0.03	0.00	0.01	0.00	0.02	0.00	0.02	0.00	0.02	0.01
Mg	0.01	0.01	0.02	0.00	0.02	0.00	0.01	0.01	0.01	0.01	0.01
$Xusp$	0.55		0.53		0.53		0.51		0.51		0.94
$Xilm$		0.89		0.91		0.91		0.91		0.89	
T, °C	953.00		919.00		905.00		912.00		940.00		
fO_2	−11.37		−12.16		−12.55		−12.20		−11.54		

$Xusp = Ti^{+4}/(Ti^{+4} + Fe^{+3}/2)$

$Xilm = Fe^{+2}/(Fe^{+2} + Fe^{+3}/2)$

Tit titanohematite, *Il* ilmenite, *Ilmo* ilmohematite (re-integrated)

took place during a deformation and metamorphic event after magmatic emplacement.

Selecting only points that overlap with concordia (1σ error ellipses), six points, mostly from the unaltered grain 3 gave a concordia age of 93.2 ± 1.7 Ma as shown in the Wetherill concordia plot (Fig. 6b). A weighted mean Th–Pb age on the same points is 91.0 ± 1.7 Ma.

The U–Pb data on zircon, monazite and xenotime for both samples are consistent and yields a combined result of 92.6 ± 1.2 Ma. This is interpreted as the age of intrusion and magmatic crystallization of the two granite samples.

Mineral Chemistry

Tourmaline

The tourmalines from the leucogranite dyke in the Mawat ophiolite, in general, belong to the alkali group, (Fig. 7a) following the classification by Hawthorne and Henry (1999). As most of the analyzed grains of tourmaline are aluminous (Al > 6.00 apfu), the X-vacancy/(Na + X-vacancy) vs. Mg/(Fe + Mg) diagram is used here for tourmaline classification. In this diagram, tourmalines from the leucogranite plot most commonly within the schorl–dravite field (Fig. 7b). Overall, the leucogranite tourmaline is Ca- and K-poor, with Na/ (Na +

Ca) typically between 0.70 and 0.99 (average: 0.88). The core to rim color variation in the coarse grain tourmaline correlates well with its major-element composition, light blue and green varieties are reduced in Ti (Fig.8), relatively rich in Fe; the Fe#(Fe/(Fe + Mg)) value is between 0.50 and 0.55 for light blue tourmaline, and greater than 0.6 for the green variety. The Li content was not determined but is considered to be negligible, as bulk-rock analyses of strongly tourmalinized rocks (up to 10 vol% tourmaline) contain less than 10 ppm Li (Kareem 2015).

Biotite

EPMA results show that the biotite in the leucogranite has bimodal chemistry. The marginal zone biotite contains high concentrations of MgO (17.2–18.4 wt%), very high levels of Al_2O_3 (19.2–20.9 %), and low FeO total (8.3–9.0 wt% with Mg/ $(Fe^{2+} + Mg)$ ratios between 0.77 to 0.78 (see Table 5). Inner zone biotites contain high FeO (16.12–17.7 wt%), very high concentrations of Al_2O_3 (19.6–20.8 wt%) and low MgO (11.1–11.8 wt%) with Mg/$(Fe^{2+} + Mg)$ ratios between 0.54 and 0.55 (see Table 5). Regarding TiO_2, pale brown biotites from the marginal zone have the lowest content (mean, 0.9 wt%) and reddish ones from the inner zone have the highest TiO_2 (mean, 2.1 wt%).
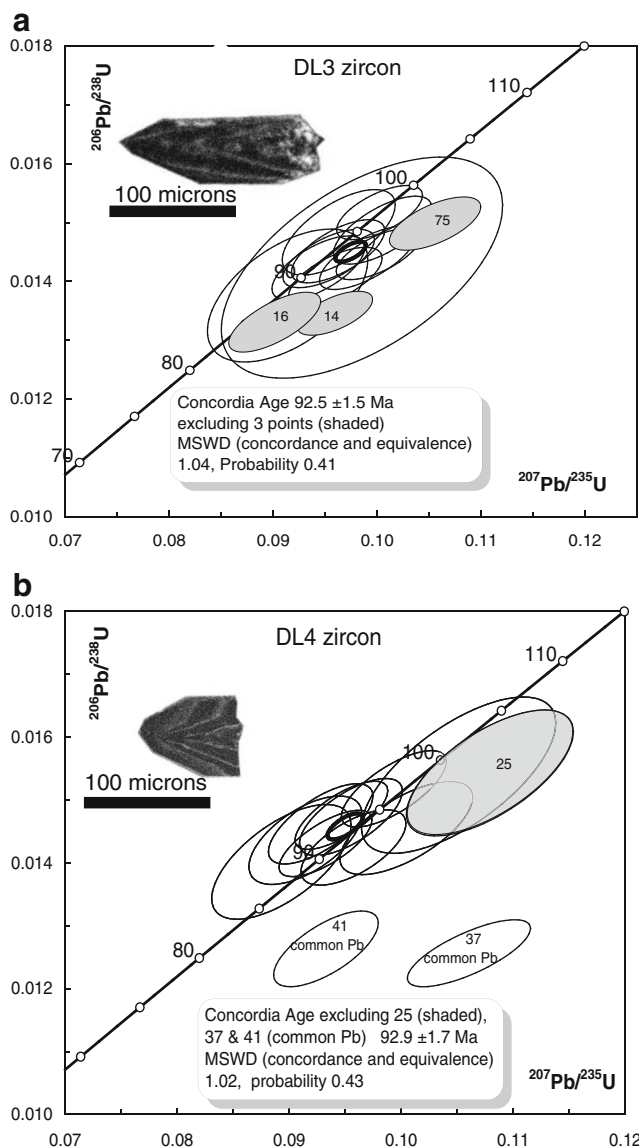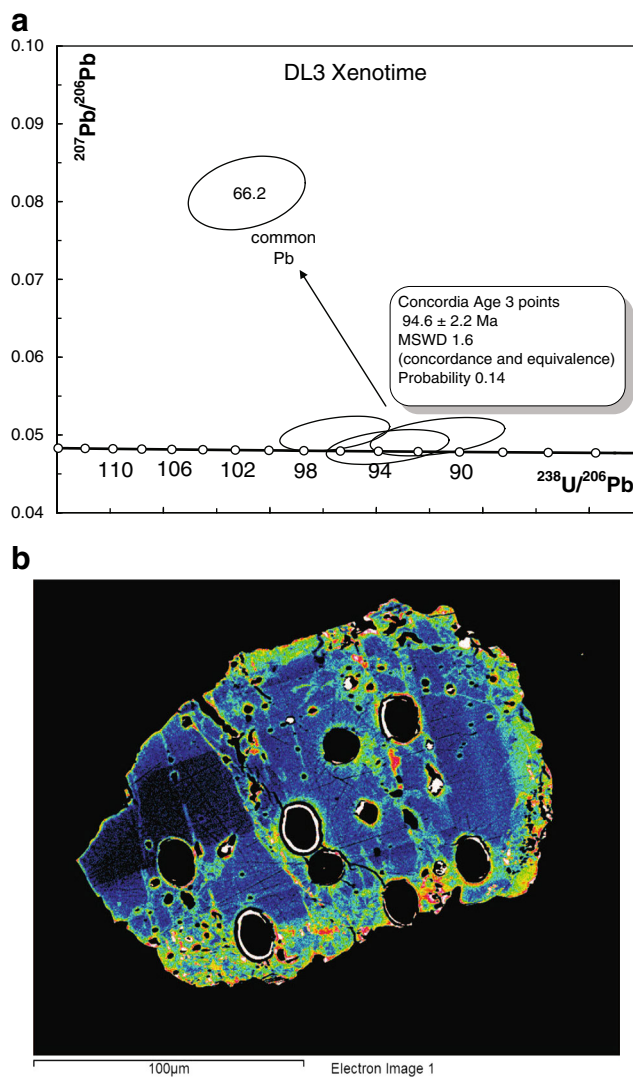
Fig. 4 a and **b** Concordia diagrams of samples DL3 and DL4 from Daraban leucogranite. Sample locations of 1 and 1.5 m from the contact, respectively
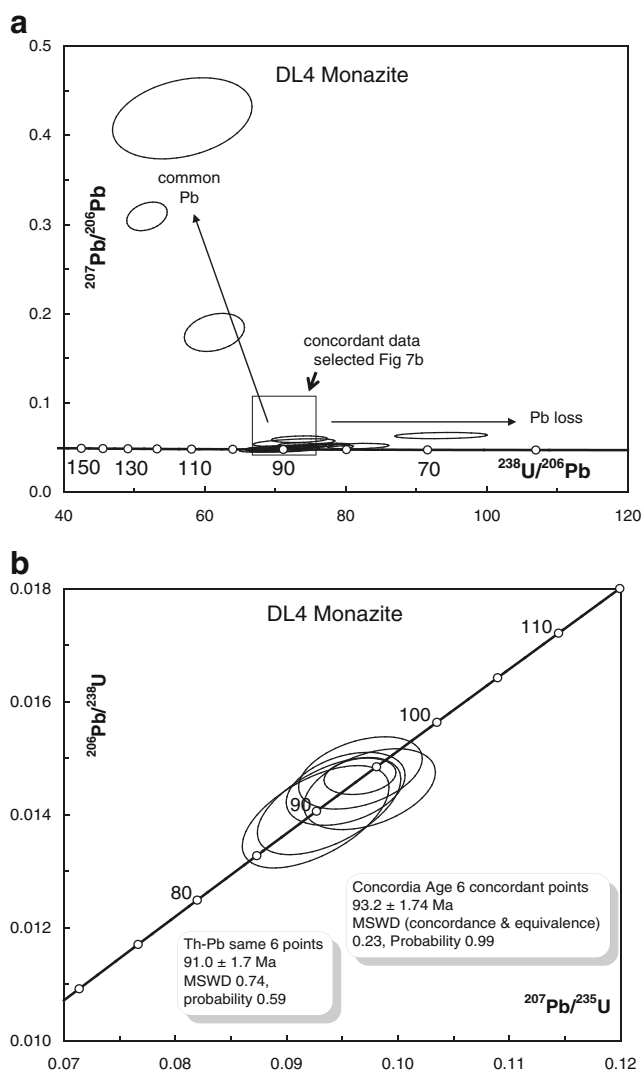

Fig. 5 a Tera-Wasserburg concordia plot of U–Pb data for xenotime from the Daraban leucogranite sample DL3 (1σ error ellipses). **b** SEM of grain 5 of sample DL4 showing Th-enriched fractures in *green*

On a Mg–(Fe^{2+} + Mn)–(Fe^{3+} + Al^{VI} + Ti) biotite classification diagram, biotites from the Daraban leucogranite are classified as phlogopite and Mg-rich biotites (Forster 1960) for marginal and inner zone respectively (Fig. 9).

Peraluminosity index (A/CNK; molar Al$_2$O$_3$/ (CaO+ Na$_2$O+K$_2$O)) of biotite shows relatively consistent A/CNK values (1.8–1.9) for biotites from the marginal and internal zones from the leucogranite indicating their aluminous character.

The most pronounced compositional characteristics of the biotite in the Daraban leucogranite intrusive suites are the similarity in Al contents and the differences in Fe/ (Fe+Mg) value. Both features are sensitive indicators of conditions in the host magma (Wones and Eugster 1965).

The similarity in total Al reflects the peraluminuos narture of the host magma and suggests that both types of biotite crystallized from the same magma. The differences in Fe/ (Fe+Mg) values of biotite from the Darban leucogranite reflect either important differences in the oxygen fugacity or Mg-diffusion from the country rock by metasomatic process.

Discussion

The implication of ages for the leucogranite

Zircon, xenotime and monazite U–(Th)–Pb dating shows consistent, concordant ages of 92.6 ± 1.2 Ma for two samples of a leucogranite dyke. Thus, the granitic rocks in Mawat ophiolite were formed simultaneously with a

Fig. 6 **a** Tera-Wasserburg concordia plot of U–Pb data for monazite from the tourmaline leucogranite sample DL4. **b** Wetherill concordia plot of U–Pb data for monazite from the tourmaline leucogranite sample DL4, selecting only points which overlap with Concordia
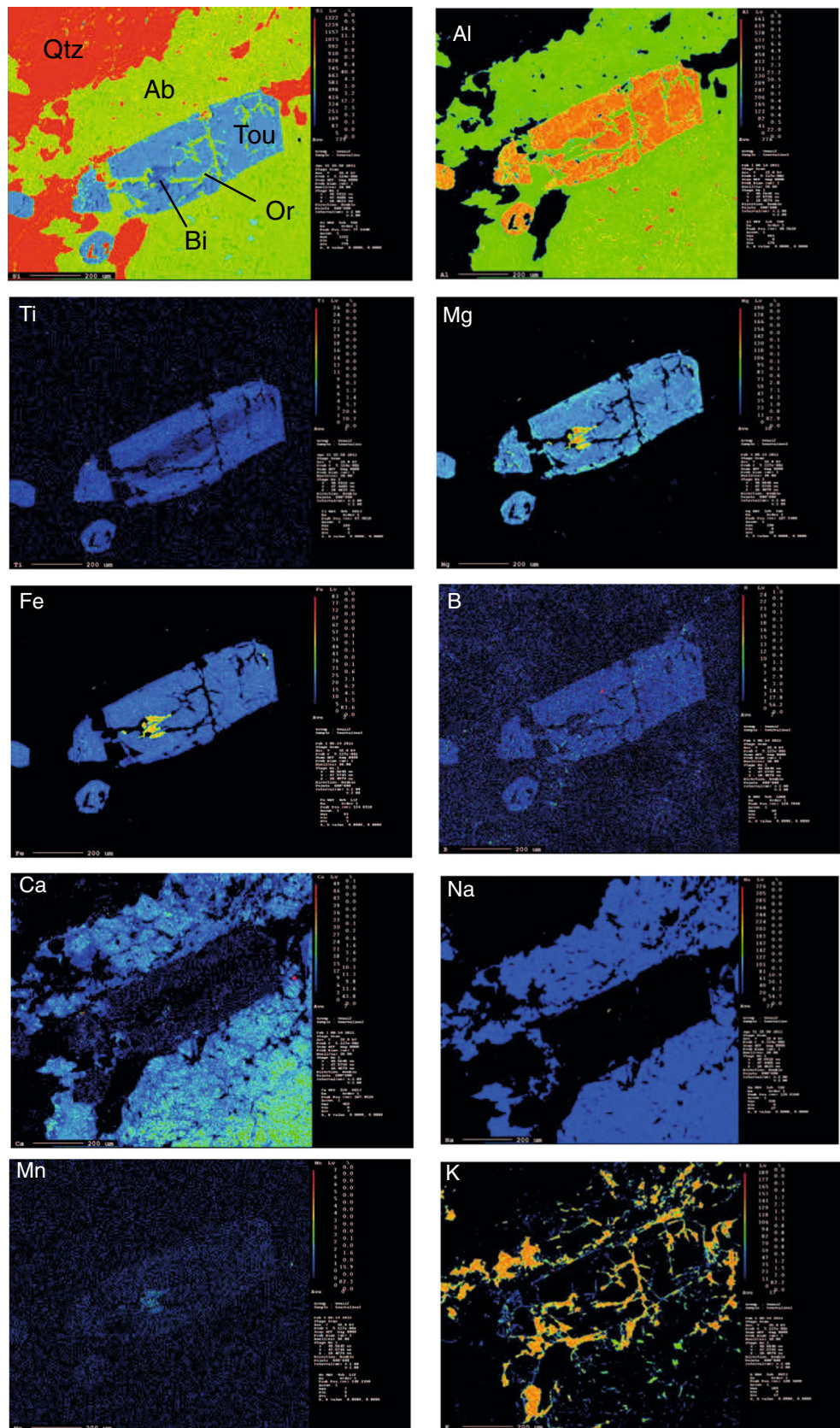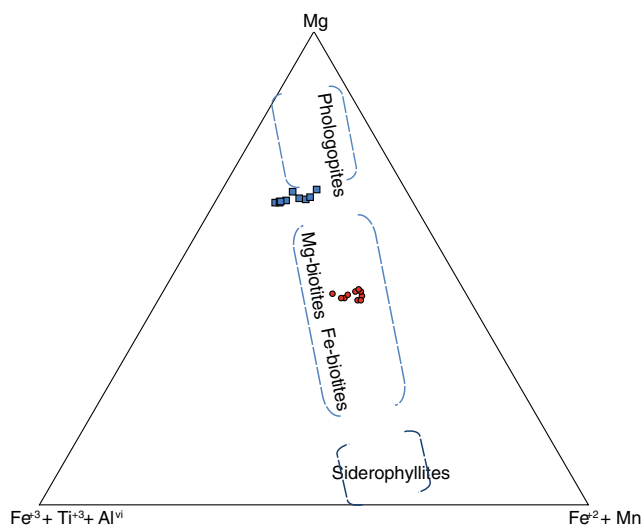
Fig. 7 **a** Classification of tourmaline from the Daraban leucogranite dyke specify on the X-site occupancy diagram from Hawthorne and Henry (1999). **b** Compositions of tourmalines from the tourmaline leucogranite (DL2 and DL3 samples) plotted in terms of X-site vacancy vs. Mg/(Mg+Fe)

regional episode of granitic intrusions in Iranian outer Zagros ophiolites (92–98 Ma: Shafaii Moghadam and Stern 2015 and references therein), Oman (93–98 Ma: Tilton et al. 1981) and Troodos ophiolites (92 Ma: Mukasa and Ludden 1987).

The overlap of the Rb–Sr mineral isochron age of 93.4 ± 5 Ma by Azizi et al. (2013) with the U–(Th)–Pb ages for the same intrusions demonstrates that Daraban leucogranite in Mawat ophiolite remained closed for Rb and Sr isotopes, after magmatic crystallization, even though all the major phases were affected by deformation. The age is 55 Ma older than the previously published age of the Daraban leucogranite obtained by ^{40}Ar–^{39}Ar muscovite dating method. The discrepancy between the U–(Th)–Pb zircon, monazite and xenotime age (92.6 ± 1.2 Ma) and the

^{40}Ar–^{39}Ar muscovite age (37.7 ± 0.3 Ma) is related to major tectonic phases that affect the isotopic system of datable phases especially radiogenic unbounded argon in muscovite.

These U–(Th)–Pb zircon, xenotime, and monazite ages are 10–15 Ma younger than published 105 ± 5 Ma K–Ar (Aswad and Elias 1988) ages for hornblende from diabasic rocks of the Mawat ophiolite and ~100 Ma Rb–Sr ages for serpentinite rocks associated with the ultramafic section of Mawat ophiolite (Aziz et al. 2011). As closure temperatures of zircon and normal igneous monazite are 900°C and 700–750 °C, respectively (Cherniak and Watson 2000; Heaman and Parrish 1991), the new U–Pb zircon, xenotime, and monazite ages are best interpreted as magmatic crystallization ages. These younger ages of Daraban leucogranite suggests that the leucogranite intrusion postdated formation ages for the mafic and ultramafic country rocks of the Mawat ophiolite.

Fig. 8 X-ray maps of euhedral tourmaline grain with fine inclusion of biotite associated with quartz + orthoclase + albite. Sample no. DL2. Abbreviation: *Bi*, biotite; *Qtz*, Quartz; *Tour*, Tourmaline; *Ab*, albite; *Or*, orthoclase.

Fig. 9 Classification of biotites from Daraban leucogranite in terms of cations per formula unit in the ternary Mg–(Fe^{+2} + Mn)–(Al^{VI} + Fe^{+3} + Ti) plot of Forster (1960)

Tourmaline chemistry versus the host rock type

The major element composition of tourmaline is strongly influenced by the host rock composition (Henry and Guidotti 1985). Henry and Guidotti's (1985) Al–Fe–Mg and Mg–Fe–Ca ternary diagrams were used to verify the type of the rock in which the tourmalines were formed.

On the Al–Fe–Mg diagram all tourmaline data plotted in the field of metapelites and metapsammites coexisting with an Al-saturating phase (field 4 of Fig. 10a).

Concerning the type of rock where the tourmalines were formed, we notice that the tourmaline rim composition plot in the fields of Li-poor granitoid (field 2 of Fig. 10b) while the cores plot in those of Ca-poor metapelites, metapsammites, and quartz-tourmaline rocks (field 4 of Fig. 10b).

The Fe# value of tourmaline from the Draban leucogranite range from 0.55 to 0.61, overlapping with the Fe# of tourmaline in metasedimentary rocks.

Tourmalines from granites and metasedimentary rocks have Fe# values ranging from 0.86 to 0.96 and 0.41 to 0.67, respectively (Henry and Guidotti 1985; Henry and Dutrow 1996). The tourmaline chemical data from the Daraban leucogranite suggest that the parental material of the leucogranite may have been derived from sedimentary material without undergoing an extensive fractionation process. The co-occurrence of emery sedimentary enclave within the Daraban leucogranite may support less differentiation (Mohammad et al. 2014).

Biotite chemistry versus the host rock type

The major oxide composition of biotites is routinely used as a guide to evaluate the physicochemical conditions in which their magmatic host-rocks were formed. The conditions include oxygen fugacity in the parent magmas (Wones and Eugster 1965), granite liquidus temperature (Abbot and Clarke 1979), to classify the granitoid (Abdel-Rahman 1994) as well as to date the crystallization history and tectonic events registered by these rocks. Abdel-Rahman (1994) discriminated three compositionally distinct fields of biotite
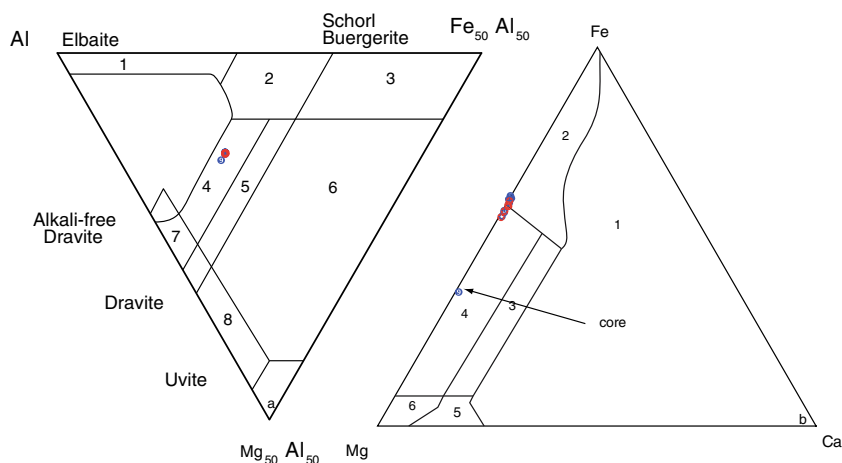
Fig. 10 **a** Al–Fe–Mg plots for tourmalines from Daraban leucogranite dyke after Henry and Guidotti (1985) fields (*1*) Li-rich granitoid pegmatites and aplites, (*2*) Li-poor granitoids and their associated pegmatites and aplites, (*3*) Fe^{+3}-rich quartz-tourmaline rocks (hydrothermally altered granites), (*4*) metapelites and metapsammites co-existing with an Al-saturating phase, (*5*) metapelites and metapsammites not coexisting with an Al-saturating phase, (*6*) Fe+3-rich quartztourmaline rocks, calc-silicate rocks and metapelites, (*7*) low-Ca metaultramafics and Cr, V-rich metasediments, (*8*) metacarbonates and metapyroxenites, Ca-poor metapelites metapsammites and quartz-tourmaline rocks. **b** Mg–Fe–Ca cation plots for tourmalines from Daraban leucogranite dyke after Henry and Guidotti (1985) fields (*1*) Li-rich granitoid pegmatites and aplites, (*2*) Li-poor granitoids and their associated pegmatites and aplites, (*3*) Ca-rich metapelites, metapsammites, and calc-silicate rocks, (*4*) Ca-poor metapelites metapsammites and quartz-tourmaline rocks, (*5*) metacarbonate, (*6*) metaultramafic

based on major oxides that reflect different magmatic host rocks: alkaline (I-type), calc-alkaline (I-type), and peraluminous (I-type and S-type).

Biotite is the most common mineralogical sink for excess aluminum in granite generally and particularly in the Darban leucogranite. This is demonstrated in Fig. 11a, in which the biotites have almost twice the whole-rock peraluminosity index in the Daraban leucogranite. Whalen and Chappell (1988) documented that Al^{VI} abundances in biotite permit discrimination between I- and S-type granites, thus biotite in I-type granites are characterized by low Al^{VI} abundances (<0.4 apfu), whereas biotite hosted in S-type granite has higher Al^{VI} abundances (0.2–0.7 apfu).

Taking this characteristic of biotite into consideration, we compiled a database of biotite from 29 localities based on more than 31 references (Lalonde and Bernard 1993; Abdel-Rahman 1994 and references therein; Villaseca and Barbero 1994; Aydin et al. 2003; Shabani et al. 2003; Koh and Yun 1999) in attempt to distinguish between biotite from S- and I-type granites, using the ACNK vs Al_2O_3 criteria of biotites. In

Fig. 11b, these data show that biotite from I-type granite and S-type granite can be distinguished. The Al^{VI} abundances in biotites from the Darban leucogranite range from 0.7 to 0.9 apfu, suggesting that the biotite in the Daraban leucogranite is of sedimentary origin.

Oxygen fugacity

Biotite

Biotite composition is a valid recorder for the oxidation state of the magma from which it crystallized when it coexists with K-feldspar + magnetite. Wones and Eugster (1965) applied the composition of biotite solid solutions in the ternary system annite $KFe_3^{2+}AlSi_3O_{10}(OH)_2$–phlogopite $KMg_3AlSi_3O_{10}(OH)_2$–siderophyllite $KFe_3^{3+}AlSi_3O_{10}(OH)_2$ for the approximation of oxygen fugacity by using a variety of oxygen buffers. In Fig. 12a, the biotites cluster into two separate regions.

Fig. 11 **a** Plot of A/CNK value of biotite vs. whole-rock values for the leucogranite dyke studied. The whole rock samples A/CNK data is from Mohammad et al. (2014). **b** Al_2O_3 vs A/CNK for biotite in S and I type granites
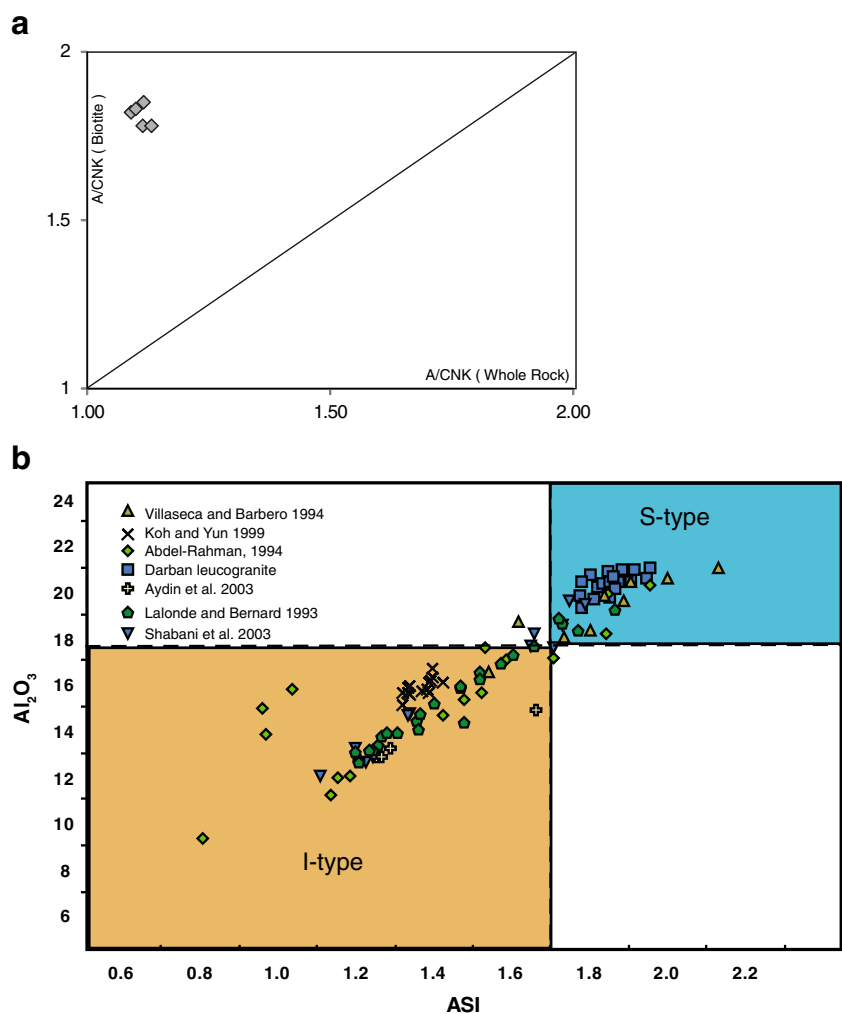
Fig. 12 a Composition of biotites in Fe^{+2}–Fe^{+3}–Mg ternary diagram along with the fO_2 buffers of Wones and Eugster (1965). **b** Composition of Daraban leucogranite biotites in the $10*TiO_2$–FeOtot–MgO ternary diagram after (Nachit et al. 2005)
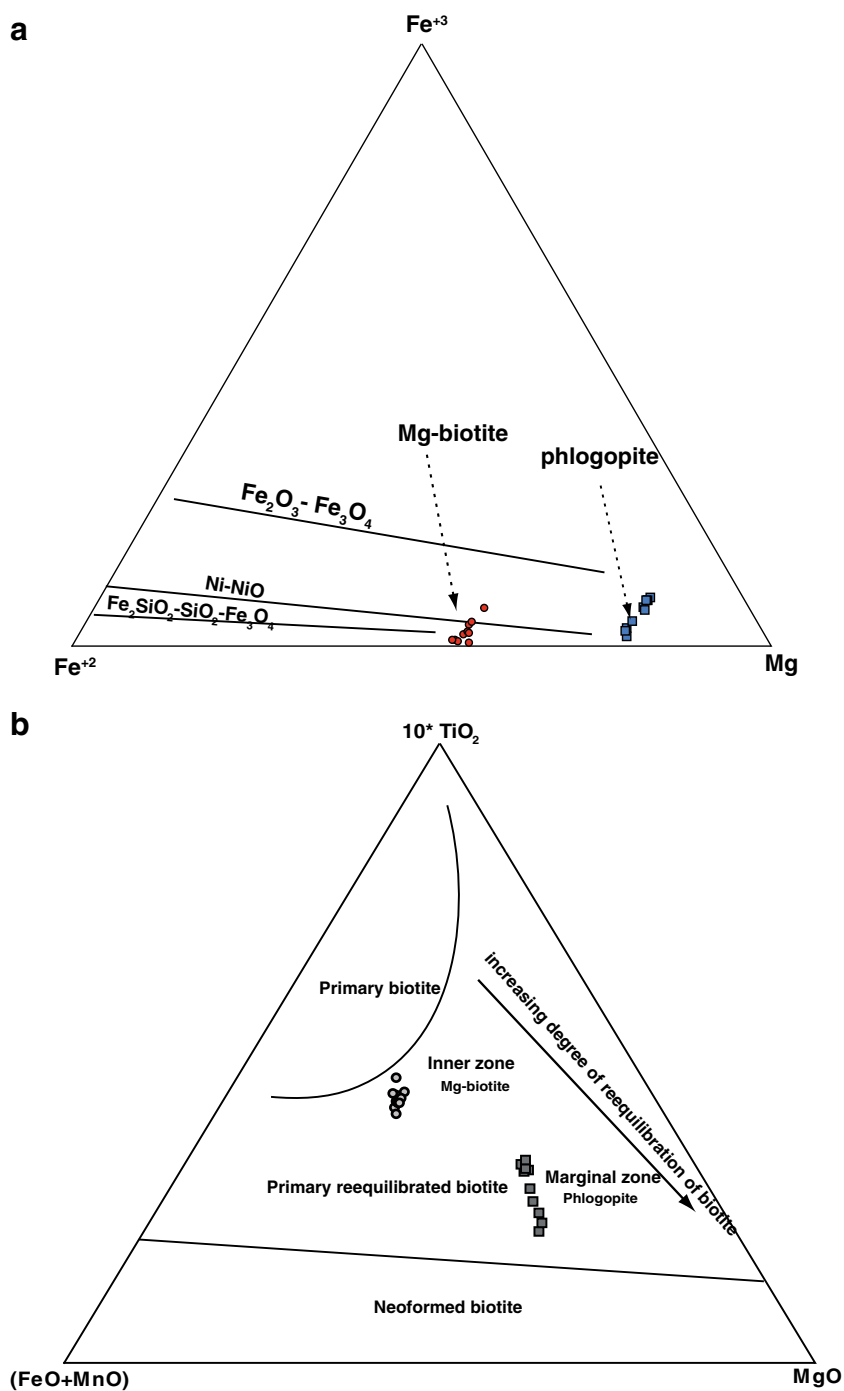
The marginal zone biotite (phlogopite) falls between the nickel oxide (NNO) and hematite–magnetite (HM) buffers, indicating somewhat oxidizing conditions similar to magnetite-series granites (Ishihara 1977). The inner zone biotite plots between the quartz–fayalite–magnetite QFM and NNO buffers (Fig. 12a) similar to ilmenite-series granites in Japan (Ishihara 1977), indicating reducing conditions.

This difference in oxygen fugacity can be supported by the unique occurrence of ilmenite oxy exsolution lamellae in titanohematite as the opaque phase in the leucogranite rock samples. A qualitative estimate of oxygen fugacity and temperature can be obtained from the Fe/(Fe + Mg) value of biotite by applying the calibrated curve of Wones and Eugster (1965) in fO_2–T space for the biotite + K-feldspar + magnetite equilibrium. A Crystallization temperature of 900 to 1100 °C for Mg–biotite and phlogopite in Daraban leucogranite is obtained, estimated log fO_2 values span a range of 10^{-10} to 10^{-13} bars. Values for T and fO_2 of individual

biotite are presented in Table 5 based on Fe/(Fe + Mg) value of biotite. The data apparently suggest that the phlogopite is the early phase that crystallized first, whereas the Mg–biotite crystallized later. However on 10*TiO$_2$–FeO–MgO ternary diagram of Nachit et al. (2005) the biotites in Daraban leucogranite plot in the field of re-equilibrated primary biotite with Mg–biotite closer to primary biotite field(Fig. 12b). This suggests that the marginal zone biotite extensively re-equilibrated with physicochemical conditions in the host rock as a result of Mg-cryptic metasomatism from mantle host rock.

Fe–Ti Oxides

The equilibrium between the iron–titanium oxide minerals has been widely engaged to give a quantitative thermo-oxy barometer in various igneous and metamorphic rocks (Buddington and Lindsley 1964; Sauerzapf et al. 2008). Our SEM/electron probe analyses of titanohematite and ilmenite in the exsolution intergrowths, illustrated in Fig. 13a, b, c, d, showed that their compositions are consistent, suggesting that exsolution took place at a high temperature which then cooled rapidly. Based on the experimental works of Buddington and Lindsley (1964) and Sauerzapf et al. (2008), the compositions of co-existing Fe–Ti oxides in the exsolution intergrowths in leucogranite samples were used to measure fO$_2$ and T. Magnetite–ilmenite geothermobarometry (Lepage 2003) and isopleth diagrams of Xusp-Xilm (Sauerzapf et al.

2008) were used for quantitating fO$_2$ and T in Daraban leucogranite. The results are presented in Table 5 and Fig. 14. The obtained results of fO$_2$ and T overlap with the results of Mg–biotite using biotite crystal chemistry in Table 5. This suggests that the parental hemoilmenite was exsolved at ~900 °C to produce exsolution of ilmenite (X$_{il}$ = 0.90)–Ti-rich hematite (Xusp = 0.53).

Re-integration of exsolved Fe–Ti oxides was done using the compositions of the two unmixed phases of sufficiently coarse grains comprising lamellae of ilmenite in titanohematite, analyzed by electron microprobe. The proportions of the exsolution lamellae and host were estimated for four rock samples by computer image analysis of back-scattered electron (BSE) images. The bulk of ilmohematite has Xusp of 0.94 ± 0.02 which may suggest an extreme crystallization temperature of more than 1,300 °C (Tauxe 2010; Sauerzapf et al. 2008). The Fe–Ti oxide exsolution can be explained based on the following reaction:

$$\text{Hemoilmenite} = \text{Ilmenite} + \text{Titanohematite}$$
$$3\left(\text{Fe}_{2-y}\text{Ti}_y\text{O}_3\right) = 2\text{FeTiO}_{3\ (\text{ilmenite})} + \text{Fe}_{2-y}\text{Ti}_y\text{O}_{3\ (\text{titanohematite})}$$
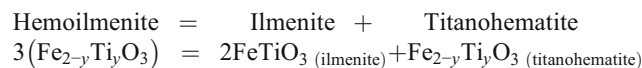
Solidification pressure

We have used biotite chemistry to estimate the pressure and depth of crystallization of the tourmaline leucogranite

Fig. 13 **a**, **b**, **c** and **d** BSE images of ilmenite-titanohematite exsolution from Daraban leucogranite samples (DL3 and DL5) used for re-integration of ilmohematite composition (0.4 ± 0.03 ilmenite + 0.6 ± 0.03 titanohematite). *Light gray color* = titanohematite, dark gray = ilmenite
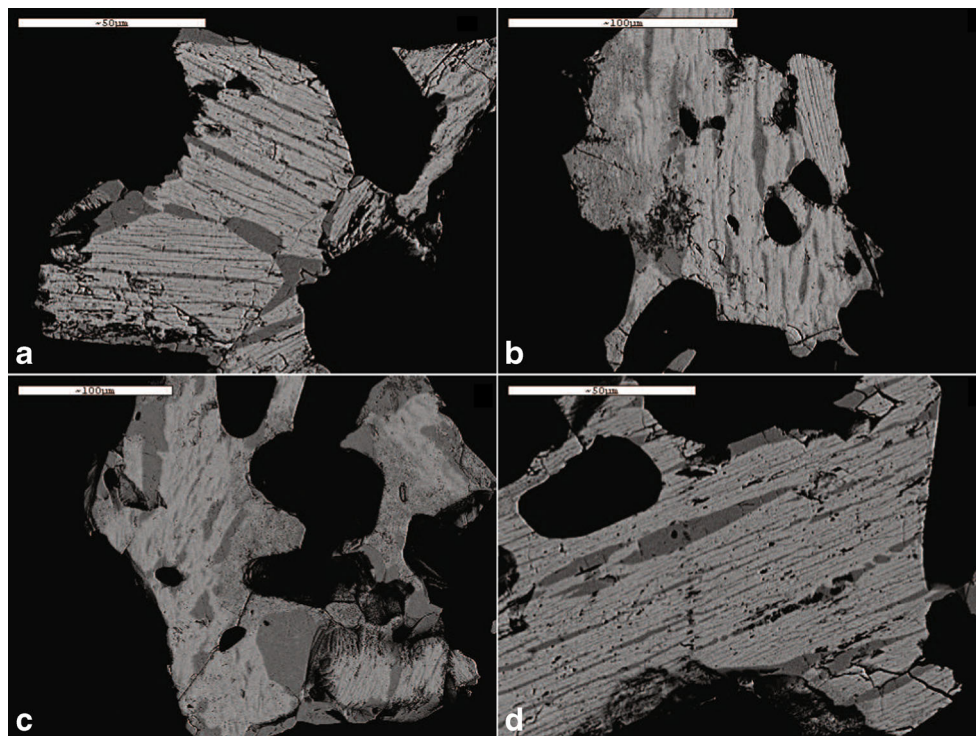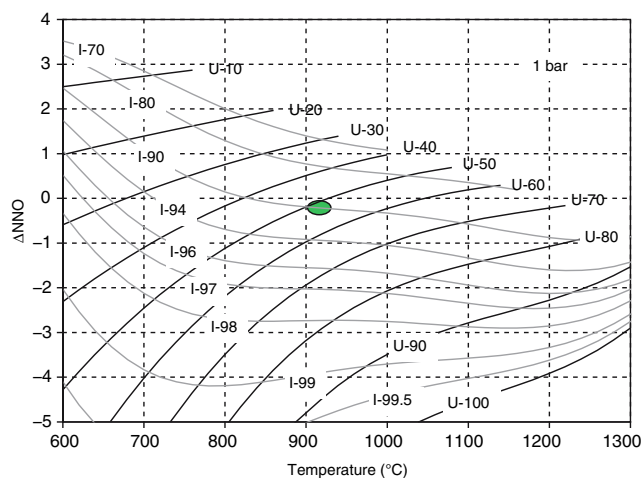
Fig. 14 Composition of Fe–Ti oxides in isopleths of X*usp* vs X*ilm* of as a function of temperature and oxygen fugacity (ΔNNO) after Sauerzapf et al. (2008)

dyke. From the chemical data of biotite (see Table 4), it is clear that the Al_2O_3 contents of Mg–biotite and phlogopite are nearly equal (see Table 4); thus it is feasible to use Al contents as guide to estimate the pressure of solidification (Etsuo et al. 2007). The solidification pressure of the granitic rocks shows a positive correlation with increasing ^TAl in biotite, thus the total Al content in biotite ($Al^{IV} + Al^{VI}$) can be used to quantify the solidification pressure as a dependable geobarometer. The equation proposed by Etsuo et al. (2007) was used to calculate the crystallization pressure and depth, with the crystallization depth estimated from a pressure–depth relationship of 1 kbar to 3.3 km depth:

The following equation was used to calculate the biotite crystallization pressure

$$P\,(Kbar) = 3.03 \times {}^TAl - 6.53\,(\pm 0.33)$$

where ^TAl is the total aluminum content of biotite calculated on the basis of 22 oxygen atoms. The crystallization pressures of biotite in the tourmaline leucogranite dyke are given in Table 5. As the ^TAl for the phlogopite (Avg.^TAl = 3.42 apfu) and Mg-rich biotite (Avg.^TAl = 3.56 apfu) is nearly the same, the crystallization pressures range from 3.8 to 4.2 kbar, corresponding to average depths of 12.5–13.8 km.

Tectonic setting

Biotite signature

Biotite compositions from divers granitic rocks based on a large data set have been used by Abdel-Rahman (1994) to discriminate between (1) anorogenic extension-related peralkaline granites, (2) calc-alkaline I-type orogenic suites and (3) peraluminous rocks including S-type granites.

Several diagrams were introduced to distinguish these different tectonic settings. We used the ternary FeO*–MgO–Al_2O_3 plot shown in Fig. 15, which is probably the most powerful discriminant since it reflects changes in redox state and peraluminosity. Biotite compositions from rocks of the Darban leucogranite dyke marginal zone fall principally in the subduction-related calc-alkaline field, whereas those from the inner zone plot in the collisional related peraluminous field (Fig. 15).

Tourmaline signature

The most common tourmaline-bearing granite is one that has undergone significant fractionation, because boron, an essential constituent of tourmaline, behaves incompatibly in igneous systems and is therefore highly enriched in fractionated melts (London 1999). Tourmaline is most common in calc-alkaline and peraluminous granites. If granitic rocks are derived from the melting of metasedimentary material that is commonly enriched in B compared to the average crust, tourmaline may occur in substantial modal amounts.

Igneous tourmaline tracks the composition and mineral assemblage of its host magma. Therefore, it provides a first-order approximation of the composition of the magma from which it nucleated, including changes in major components such as Fe, Mg, and Mn (Jolliff et al. 1986). In general Na-rich tourmaline with intermediate Fe and Mg is diagnostic for intermediate igneous rocks, e.g., schorl and dravite, whereas tourmaline from moderately fractionated granitic rocks tends to be Fe-rich (i.e., schorl and foitite; see nomenclature in Hawthorne and Dirlam 2011). With increased fractionation,
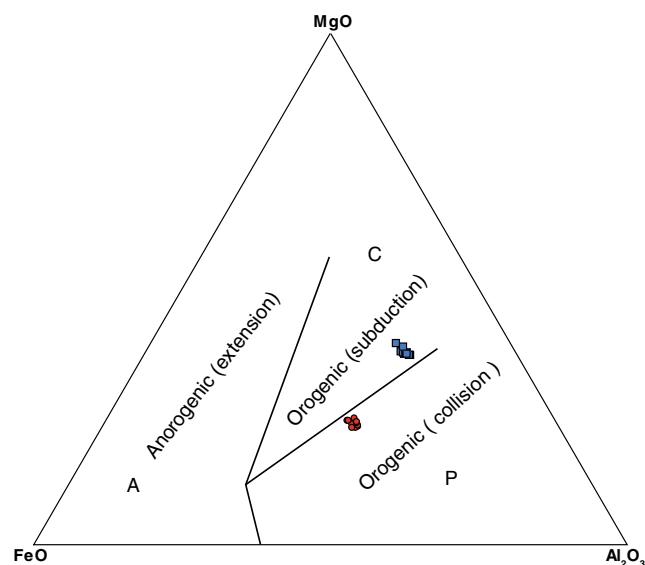
Fig. 15 Composition of biotite from Daraban leucogranite dyke expressed in the discrimination plot of Abdel-Rahman (1994). *A*: alkaline, *C*: calc-alkaline, and *P*: peraluminous granite fields. FeO* = [FeO + (0.89981*Fe_2O_3)]

tourmaline gets enriched in Li, so that in highly differentiated pegmatites, the Li species elbaite, fluor-liddicoatite, and rossmanite are characteristic.

Tourmaline is identical phase for the B-enriched group of granitic-pegmatites of the lithium–caesium–tantalum (LCT) family, typically formed at the expense of metasedimentary materials and occurs more rarely in granitic pegmatites that represent the culmination of protracted fractional crystallization of basaltic magma of the niobium–yttrium–fluorine (NYF) family (London 2008). Martin and De Vito (2005) consider that LCT granite-pegmatites are members of orogenic (calc-alkaline) suites formed in a subduction setting. In contrast, NYF granite–pegmatites are affiliated with anorogenic suites, formed in an extensional setting. The Al and Na-rich dravite–schorl nature of tourmaline from the Daraban leucogranite dyke, together with mantle host rock that suggests the leucogranite dyke was formed in the subduction zone tectonic environment of the Mawat ophiolite.

Petrogenesis

Granitic rocks within ophiolites can be grouped into two main genetic categories: (1) Na-rich granite (trondhjemites) are generated either by extensive fractional crystallization of basaltic magma at high levels (i.e., at low pressure) or by hydrous partial melting of gabbros or MORB in subduction zones (Koepke et al. 2004, 2007); (2) K-rich granite (leucogranites) are generated by partial melting of sediments in subduction zones (Cox et al. 1999; Haase et al. 2015).

Because the Daraban leucogranite is dominated by K-rich minerals such as muscovite, orthoclase and minor biotite, the possibility that the Daraban leucogranites represent fractional crystallization of mafic magmas in the crust of the Mawat ophiolite was rejected because this process will yield sodium-rich and potassium-depleted phases in the felsic magma in ophiolites.

The peraluminous nature of biotite and tourmaline, occurance of phlogopite and major element composition of the host leucogranite mantle intrusive with >72 wt% SiO_2 (Table 1 in Mohammad et al. 2014) closely resembles that of rocks produced by anatexis of subducted pelagic sediments at <900 °C, depth 70–90 km in the stability field of phlogopite (Wyllie and Sekine 1982; Johnson and Plank 1999; Hermann and Spandler 2008). Also, the similarity of the incompatible elements and especially the boron composition of the most SiO_2-rich rocks to the Himalayan and Oman leucogranites imply that these rocks represent partial melts of sediments along the subduction zone. The source or the magma might be related to seafloor sediments rich in silica and depleted in calcium that suffered anatexis during their subduction into deeper regions. The obtained physicochemical conditions suggest a transition from the high temperature moderately oxidizing environment to low temperature reducing

environment. This supports the idea of formation of granitic melt along the deep subduction zone followed by upward movement of the melt into a reducing environment in the mantle wedge at shallower depths. This mantle section in Mawat ophiolite probably represents the tip of the mantle wedge of the former subduction zone and must have been relatively hot to allow equilibration of the biotite along the margin of the Daraban leucogranite through Mg metasomatic process.

A model to explain crystallization conditions

Experimental studies (Lattard et al. 2006; Sauerzapf et al. 2008; Yoder and Kushiro 1969; Tareen et al. 1995; Condamine and Médard 2014) show that the phlogopite and hemoilmenite are the common minerals stable under mantle oxidizing conditions along subduction zones. Fe–Ti oxides thermo-oxy barometry indicates that the first mineral crystallized was hemoilmenites. As the temperature fell and the oxygen fugacity decreased, due to upward movement along the mantle wedge, the homolimenites in the silicate melt were converted to titanohematite and ilmenite exsolution symplectites (intergrowths) at 900 °C.

However, the biotite thermometer suggest two different crystallization temperature at 1,100 and 900 °C but this is attributed to re-equilibration rather than to different crystallization conditions. The re-equilibration mechanism can be explained the three following scenarios.

Scenario 1:When the magma is rising from the melting region along the subduction zone at 70–90 km depth at 900 °C, the Mg-rich biotite starts to crystallize homogenously though out the Daraban leucogranite magma. With further upward raising of the magma into hotter mantle wedge (see Fig. 7 in Stern 2002) the marginal zone interacts with hot host rock and converts Mg-rich biotite to phlogopite through the high-temperature Mg-metasomatic process cryptic metasomatism (Fyfe and McBirney 1975; Wyllie and Sekine 1982).

Scenario 2:Following physical mechanisms by which granitic magmatic dykes crystallize when the magma chambers contain a central mass of nearly crystal-free magma that gradually loses heat and crystallizes in situ inward from its margins (Morgan and London 1999). Phlogopites phase will crystallized first at about 1,100 °C as the magma rises from the melting region along the subduction zone into the solid hot overlying mantle wedge peridotite. This process causes the crystallization of marginal phlogopite along the border of felsic melts. The phlogopite formation produces Mg-depleted and Fe-enriched toward the felsic melt internal part as consequences Mg–biotite crystallize at a higher level, lower temperature 900 °C and reducing environment.
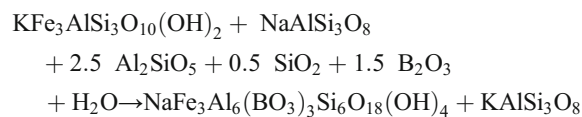
Scenario 3:Phlogopite formed along the marginal zone of leucogranite at the expense of Mg-rich biotite due to the infiltration of Mg-rich hydrothermal fluids through both the

leucogranite and serpentinite, thus the formation of phlogopite should be coeval with the serpentinization process in the country rock (Cheilletz et al. 1993).

The uniform crystal size throughout the Daraban leucogranite dyke and the lack of chilled margin excludes scenario 2. Scenario 3 is also excluded, as the serpentinization process is a low-temperature process it is unlikely to produce high temperature phlogopite along the contact between the dyke and host rock.

The high-temperature stability field of the phlogopite combined with the subduction zone characteristic of the host rock may suggest that the phlogopite formation process, through scenario 1 is more likely.

With further falling in temperature and continuing upward movement of the melt as result of buoyancy, the composition of the melt became boron saturated and peraluminous and Mg–biotite started to react with peraluminous liquid to form tourmaline. The co-occurrence of biotite + orthoclase + quartz + albite + tourmaline (Fig. 9) suggests that the biotite started to form tourmaline according to following reaction (Wolf and London 1997):

$$KFe_3AlSi_3O_{10}(OH)_2 + NaAlSi_3O_8$$
$$+ 2.5 \ Al_2SiO_5 + 0.5 \ SiO_2 + 1.5 \ B_2O_3$$
$$+ H_2O \rightarrow NaFe_3Al_6(BO_3)_3Si_6O_{18}(OH)_4 + KAlSi_3O_8$$

In general, the local occurrence of biotite as inclusions in tourmaline shows that the former started crystallizing before tourmaline (Fig. 9). It is plausible that oxidizing conditions promoted the formation of tourmaline at the expense of biotite (Scaillet et al. 1995). These observations, together with the experimental data suggests a water content in the melt at the emplacement level in the range 6.0–7.5 wt% H_2O and boron contents ranging from about 0·15 to 6 wt% B_2O_3 (Scaillet et al. 1995; Benard et al. 1985; Wolf and London 1997).

The possible sources of sedimentary rocks

Before the subduction stage during rifting in the Neo-Tethyan oceanic basin, there was a continued deposition of radiolarite facies on the oceanic crust that is one of the diagnostic features of the Neo-Tethyan Mesozoic realm. This sedimentary facies extended from Hawasina region (Oman) in the south, passed by Pichakun in south Iran, Kermanshah (western Iran), Qulqula (Kurdistan region of Iraq) and ended with Kocali basin (Turkey) (Berberian and King 1981; Ali et al. 2013). The Neo-Teythan radiolarites range in age from Triassic to Cretaceous. In Iraq, the Qulqula radiolarite comprises various lithostratigraphic units, of which the pelagic and hemipelagic facies of radiolarite deposited in the inner abyssal plain of the Neo-Tethyan oceanic basin are typical (Baziany 2014). Following the subduction, a vast amount

of radiolarite material of the Qulqula group and oceanic crust descended together along the subduction zone, reflecting typical accretionary wedges above NE subduction zone (Karim et al. 2011). Partial melting of these sediments probably generated the leucogranite magmas that intruded into hot depleted parts of the mantle wedge. The presence of corundum-bearing high-grade metapelite xenoliths in the leucogranite, in addition to the dominance of manganese and barium-bearing phases psilomelane and pyrolusite in Qulqula radiolarite may have been a significant contribution to the high concentration of Ba (avg: 219 ppm, Mohammad et al. 2014) and the existence of Mn–ilmenite (up to 1 wt% MnO) in the leucogranite dyke. Very high uranium levels ranging from 4,000 to 14,000 ppm in zircon may reflects that the black shale within pelagic facies involved during anatexis process to produce leucogranite magma.

Tectonic implications

The new U–Pb isotope data, together with widespread geochronological data of granitic rocks in Zagros ophiolite sectors of ~9,000-km Magrhebian–Alpine–Himalayan orogenic belt show that the distinctive period of granite production in ophiolite belts occurred synchronously with subduction events in the Neo-Teythan Ocean. The overlap in U–Pb zircon ages between the Mawat ophiolite with Ar–Ar age of Hassanbag ophiolite in Iraq and the ages of the end-member ophiolites of the Late Cretaceous Neo-Tethyan ophiolite belt represented by Troodos in Cyprus and Semail in Oman; suggests that subduction was concordant and predate the intrusion of granitic magma at 92–98 Ma. The overlapping of U–(Th)–Pb zircon, monazite and xeotime age of the Mawat ophiolite with entire Zagros ophiolites in Iran, occurrences of podiform chromitite bodies (Ismail et al. 2010), extreme dominance of gabbro over basalt units (Al-Saffi et al. 2012) and integrated with lack of BAB between the Mawat ophiolite and Arabian passive margin in the area (Baziany 2014) confirm the subduction characteristics over a mantle plume origin.

Conclusions

1. New LA-ICP-MS zircon U–Pb geochronological data for leucogranites in the Mawat ophiolite provides new insights into the timing of late Cretaceous subduction in Iraq which generated ophiolites along the Zagros ophiolite belt.
2. The composition of key mineral-like tourmaline, biotite, and Fe oxides can function as a tool for the classification

and petrogenetic characterization of leucogranite in ophiolite.

3. The Darban leucogranite dykes are slightly zoned; biotites compositions vary from a Mg-rich thin marginal zone towards a Fe-rich inner zone of the pluton. The lower fO_2 and temperature in the internal relative to the marginal area of the leucogranite dyke suggests that the marginal zone have been re-equilibrated with host rock conditions

4. The occurrence of bimodal Mg-rich biotites and phlogipites in the same rock type suggests that the biotite grains form at the same time under different physico-chemical condition in the magma. Consequently, it is risky to interpret single mineral chemistry without detailed geochemical and petrographic investigations of the studied minerals.

5. The Daraban leucogranite intrusions represent partial melts of Si-rich and Ca-depleted pelagic sediments similar to the Qulqula group that crystallized in the forearc mantle wedge.

References

Abdel-Rahman AM (1994) Nature of biotites from alkaline, calc-alkaline, and peraluminous magmas. J Petrol. 35:525–541

Abbot RN, Clarke BD (1979) Hypothetical liquidus relationships in the subsystem Al_2O_3–FeO–MgO projected from quartz, alkali feldspar and plagioclase for (H2O) < 1. Can Mineral. 17:549–560

Abdulla KL (2015) Petrogenesis and geochronology of plagiogranite rocks in Penjween ophiolite, Kurdistan region, NE Iraq. Unpublished M.Sc Thesis, University of Sulaimani, p 92

Aleinikoff JN, Schenck WS, Plank MO, Srogi LA, Fanning CM, Sandra L, Kamo SL, Bosbyshell H (2006) Deciphering igneous and metamorphic events in high-grade rocks of the Wilmington Complex, Delaware: Morphology, cathodoluminescence and backscattered electron zoning, and SHRIMP U-Pb geochronology of zircon and monazite. Bull. Geol. Soc. Am. 118:39–64

Aldiss DT (1978) Granitic rocks of ophiolites. Ph.D Thesis, Open University, UK

Ali SA, Buckman S, Aswad KJ, Jones BG, Ismail SA, Nutman AP (2013) The tectonic evolution of a Neo-Tethyan (Eocene–Oligocene) island-arc (Walash and Naopurdan groups) in the Kurdistan region of the Northeast Iraqi Zagros Suture Zone. Isl Arc. 22:104–125

Al-Mehidi HM (1975) Tertiary nappe in Mawat range. J. Geol. Soc. Iraq. VIII:31–44

Al-Saffi IK, Hadi A, Aqrawi AM (2012) Petrology of gabbroic rocks of Mawat ophiolite complex (central sector) NE Iraq. Iraqi bulletin of geology and mining. 8:65–85

Aswad KJ, Elias EM (1988) Petrogenesis, geochemistry and metamorphism of spilitized subvolcanic rocks, Mawat ophiolite complex, NE Iraq. Ofioliti. 13:95–109

Aydin F, Karsli O, Sadiklar M (2003) Mineralogy and chemistry of biotites from eastern pontide granitoid rocks, NETurkey: Some Petrological Implications for Granitoid Magmas. Chemie der Erde. 63:163–182

Aziz NR, Elias EM, Aswad KJ (2011) Rb-Sr and Sm-Nd isotopes study of serpentinites and their impact on the tectonic setting of Zagros suture zone, NE Iraq. Iraqi Bulletin of Geology and Mining. 7:67–75

Azizi H, Hadi A, Asahara Y, Mohammed YO (2013) Geochemistry and geodynamics of the Mawat mafic complex in the Zagros Suture zone, northeast Iraq. Cen Eur J Geosci. 5:523–537

Baziany MM (2014) Depositional systems and sedimentary basin analysis of the Qulqula Radiolarian Formation of the Zagros Suture Zone, Sulaimani Area, Iraqi Kurdistan Region. Unpublished Ph.D Thesis, University of Sulaimani, Iraq, p 198

Benard F, Moutou P, Pichavant M (1985) Phase relations of tourmaline leucogranites and the significance of tourmaline in silicic magma. J Geol. 93:271–291

Berberian M (1995) Master "blind" thrust faults hidden under the Zagros folds: active basement tectonics and surface morphotectonics. Tectonophysics. 241:193–224

Berberian M, King GCP (1981) Toward a paleogeography and tectonic evolution of Iran. Can J Earth Sci. 18:210–265

Black LP, Kamo SL, et al. (2004) Improved $^{206}Pb/^{238}U$ microprobe geochronology by the monitoring of a trace-element-related matrix effect; SHRIMP, ID-TIMS, ELA-ICP-MS and oxygen isotope documentation for a series of zircon standards. Chem Geol. 205:115–140

Buddington AF, Lindsley DH (1964) Iron-titanium oxide minerals and synthetic equivalents. J Petrol. 5:310–357

Buick IS, Lana C, Gregory C (2011) A LA-ICP-MS and SHRIMP U/Pb age constraint on the timing of REE mineralisation associated with Bushveld granites. S Afr J Geol. 114:1–14

Burkhard DJM (1991) Temperature and redox path of biotite-bearing intrusives: a method of estimation applied to S- and I-type granites from Australia. Earth Planet Sci Lett. 104:89–98

Burkhard DJM (1993) Biotite crystallization temperatures and redox states in granitic rocks as indicator for tectonic setting. Geol Mijnbouw. 71:337–349

Cherniak DJ, Watson EB (2000) Pb diffusion in zircon. Chem Geol. 172: 5–24

Cheilletz A, Féraud G, Giuliani G, Ruffet G (1993) Emerald dating through $^{40}Ar/^{39}Ar$ step–heating and laser spot analysis of syngenetic phlogopite. Earth Planet Sci Lett. 120:473–485

Coleman RG, Peterman ZE (1975) Oceanic plagiogranite. J Geophy Res 80:1099–1108

Condamine P, Médard E (2014) Experimental melting of phlogopite-bearing mantle at 1 GPa: Implications for potassic magmatism. Earth Planet Sci Lett. 397:80–92

Cornell DH, Brander L, Zack T, Kristoffersen M (2013) The Plat Sjambok Anorthosite and its tonalitic country rocks: Mesoproterozoic pretectonic intrusions in the Kaaien Terrane, Namaqua–Natal Province, Southern Africa. Int Geol Rev. 55: 1471–1489

Cox J, Searle M, Pedersen R (1999) The petrogenesis of leucogranitic dykes intruding the northern Semail ophiolite, United Arab Emirates: field relationships, grochemistry and Sr/Nd isotope systematics. Contrib Mineral Petrol. 137:67–287

Dodson MH, Mcclelland-Brown E (1985) Isotopic and paleomagnetic evidence for rates of cooling, uplift and erosion. Geological Society Memorier. 10:315–325

Dyar MD, Taylor ME, Lutz TM, Francis CA, Guidotti CV, Wise M (1998) Inclusive chemical characterization of tourmaline:

Mössbauer study of Fe valence and site occupancy. Am Mineral. 83: 848–864

Dymek RF (1983) Titanium, aluminum and interlayer cation substitutions in biotite from high-grade gneisses, West Greenland. Am Mineral. 68:880–899

Etsuo U, Sho E, Mitsutosh M (2007) Relationship between solidification depth of granitic rocks and formation of hydrothermal ore deposits. Resource Geology. 57:47–56

Forster MD (1960) Interpretation of the composition of tri octahedral mica. US Geol Surv Prof Pap. 354:1–48

Fuchs Y, Lagache M, Linares J (1998) Fe-tourmaline synthesis under different T and fO_2 conditions. Am Mineral. 83:525–534

Fyfe W, McBirney A (1975) Subduction and the structure of andesite volcanic belts. Am J Sci. 275-A:285–297

Gasquet D, Bertrand JM, Paquette JL, Lehmann J, Ratzov G, De Ascenção Guedes R, Tiepolo M, Boullier AM, Scaillet S, Nomade S (2010) Miocene to Messinian deformation and hydrothermal activity in a pre-Alpine basement massif of the French western Alps: new U-Th-Pb and argon ages from the Lauzière massif. Bull Soc Géol France. 181:227–241

Haase KM, Freund S, Koepke J, Hauff F, Erdmann M (2015) Melts of sediments in the mantle wedge of the Oman ophiolite. Geol. 43: 275–278

Hacker B, Mosenfelder JL, Gnos E (1996) Rapid emplacement of the Oman ophiolite: thermal and geochronologic constraints. Tectonics. 15:1230–1247

Hawthorne FC, Dirlam DM (2011) Tourmaline the indicator mineral: from atomic arrangement to Viking navigation. Elements. 7:307–312

Hawthorne FC, Henry DJ (1999) Classification of the minerals of the tourmaline group. Eur J Mineral. 11:201–215

Heaman L, Parrish R (1991) U-Pb geochronology of accessory minerals. In: Heaman L, Ludden JN (eds) Short course handbook on applications of radiogenic isotope systems to problems in geology, Mineralogical Association of Canada, pp. 59–102

Hermann J, Spandler C (2008) Sediment melts at sub-arc depths: an experimental study. J Petrol. 49:717–740

Henry DJ, Dutrow BL (1996) Metamorphic tourmaline and its petrologic applications. In: Grew ES, Anovitz LM (eds) Boron: Mineralogy, Petrology and Geochemistry, Rev Mineral, vol 33, pp. 503–557

Henry DJ, Guidotti CV (1985) Tourmaline as a petrogenetic indicator mineral: An example from the staurolite-grade metapelites of NW Maine. Am Mineral. 70:1–15

Ishihara S (1977) The magnetite-series and ilmenite-series granitic rocks. Mining Geol. 27:293–305

Ismail SA, Mirza T, Carr P (2010) Platinum-group elements geochemistry in podiform chromitites and associated peridotites of the Mawat ophiolite, northeastern Iraq. J Asian Earth Sci. 37:31–41

Jackson S, Pearson NJ, Griffin WL, Belousova EA (2004) The application of laser ablation-inductively coupled plasma-mass spectrometry to in situ U–Pb zircon geochronology. Chem Geol. 211:47–69

Jolliff BL, Papike JJ, Shearer CK (1986) Tourmaline as a recorder of pegmatite evolution: Bob Ingersoll pegmatite, Black Hills, South Dakota. Am Mineral. 71:472–500

Johnson MC, Plank T (1999) Dehydration and melting experiments constrain the fate of subducted sediments. Geochem Geophys. doi:10.1029/1999GC000014

Kareem HJ (2015) Mineralogy and geochemistry of felsic pegmatite from Mawat ophiolite, Kurdistan region, northeastern Iraq. Unpublished M.Sc Thesis, University of Sulaimani, p 151

Karim KH, Koyi H, Baziany MM, Hessami K (2011) Significance of angular unconformities between Cretaceous and Tertiary strata in the northwestern segment of the Zagros fold– thrust belt, Kurdistan Region, NE Iraq. Geol Mag. 148:925–939

Karaoğlan F, Parlak O, Klotzi U, Thoni M, Koller F (2012) U–Pb and Sm–Nd geochronology of the ophiolites from the SE Turkey.

Implications for the Neotethyan evolution. Geodinamica Acta. 25: 146–161

Koepke J, Feig ST, Snow J, Freise M (2004) Petrogenesis of oceanic plagiogranites by partial melting of gabbros: an experimental study. Contrib Mineral Petrol. 146:414–432

Koepke J, Berndt J, Feig ST, Holtz F (2007) The formation of SiO_2-rich melts within the deep oceanic crust by hydrous partial melting of gabbro. Contrib Mineral Petrol. 153:67–84

Koh JS, Yun SH (1999) The compositions of biotite and muscovite in the Yuksipryeong two-mica granite and its petrological meaning. Geosciences Journal. 3:77–86

Lalonde AE, Bernard P (1993) Composition and color of biotite from granites: two useful properties in the characterization of plutonic suites from the Hepburn Internal Zone of Wopmay Orogen, Northwest Territories. Can Mineral. 31:203–217

Lattard D, Engelmann R, Kontny A, Sauerzapf U (2006) Curie temperatures of synthetic titanomagnetites in the Fe–Ti–O system: effects of compositions, crystal chemistry, and thermomagnetic methods. J Geophys Res 111:B12S28. doi:10.1029/2006JB004591

Lepage LD (2003) ILMAT: an Excel worksheet for ilmenite–magnetite geothermometry and geobarometry. Comput Geosci. 29:673–678

London D (1999) Stability of tourmaline in peraluminous granite systems: the boron cycle from anatexis to hydrothermal aureoles. Eur J Mineral. 11:253–262

London D (2008) Pegmatites. Can Mineral Special Publication 10, p 368

Ludwig KR (2003) Isoplot/EX version 3.0, A geochronological toolkit for Microsoft Excel: Berkeley Geochronology Center Special Publication

Martin RF, De Vito C (2005) The patterns of enrichment in felsic pegmatites ultimately depend on tectonic setting. Can Mineral. 43: 2027–2048

Mohammad YO, Cornell DH, Qaradaghi JH, Mohammad FO (2014) Geochemistry and Ar–Ar muscovite ages of the Daraban Leucogranite, Mawat Ophiolite, Northeastern Iraq: implications for Arabia–Eurasia continental collision. J Asian Earth Sci. 86: 151–165

Morgan GB, London D (1999) Crystallization of the little three layered pegmatite-aplite dike, Ramona District, California. Contrib Mineral Petr. 136:310–330

Mukasa S, Ludden J (1987) Uranium-lead isotopic ages of plagiogranites from the Troodos ophiolite, Cyprus, and their tectonic significance. Geol. 15:825–828

Nachit H, Ibhi A, Abia EH, Ohoud MB (2005) Discrimination between primary magmatic biotites, re-equilibrated biotites and neoformed biotites. C R Geosci. 337:1415–1420

Payne JL, Hand M, Barovich KM, Wade BP (2008) Temporal constraints on the timing of high-grade metamorphism in the northern Gawler Craton: implications for assembly of the Australian Proterozoic. Aust J Earth Sci. 55:623–640

Rollinson H (2009) New models for the genesis of plagiogranites in the Oman Ophiolite. Lithos. 112:603–614

Sauerzapf U, Lattard D, Burchard M, Engelmann R (2008) The titanomagnetite–ilmenite equilibrium: new experimental data and thermo-oxybarometric application to the crystallization of basic to intermediate rocks. J Petrol. 49:1161–1185

Scaillet B, Pichavant M, Roux J (1995) Experimental crystallization of leucogranite magmas. J Petrol. 36:663–705

Shabani AA, Lalonde AE, Whalen JB (2003) Composition of biotite from granitic rocks of the Canadian Appalachian: a potential tectonomagmatic indicator? Can Mineral. 41:1381–1396

Shafaii Moghadam H, Stern RJ (2015) Ophiolites of Iran: keys to understanding the tectonic evolution of SW Asia: (II) Mesozoic ophiolites. J Asian Earth Sci. 100:31–59

Slama J, Kosler J, et al. (2008) Plesovice zircon—a new natural reference material for U-Pb and Hf isotopic microanalysis. Chem Geol. 249:1–35

Speer JA (1984) Mica in igneous rocks. In: Bailey SW (ed) Micas. Rev Mineral Soc Am, vol 13, pp. 299–356

Stern RA, Amelin Y (2003) Assessment of errors in SIMS zircon U-Pb geochronology using a natural zircon standard and NIST SRM 610 glass. Chem Geol. 197:111–146

Stern RJ (2002) Subduction zones. Rev. Geophys. 40. doi:10.1029/2001 RG000108

Tareen JAK, Keshava Prasad AV, Basavalingu B, Ganesha AV (1995) The effect of fluorine and titanium on the vapour-absent melting of phlogopite and quartz. Mineral Mag. 59:566–570

Tauxe L (2010) Essentials of Paleomagnetism. University of California Press, USA

Tilton GR, Hopson CA, Wright JE (1981) Uranium–lead isotopic ages of the Samail ophiolite, Oman, with applications to Tethyan Ocean. J Geophy Res. 86:2763–2775

Torres-Ruiz J, Pesquera A, Gil-Crespo PP, Velilla N (2003) Origin and petrogenetic implications of tourmaline-rich rocks in the Sierra Nevada (Betic Cordillera, Southeastern Spain). Chem Geol. 197: 55–86

Villaseca C, Barbero L (1994) Chemical variability of Al-Ti-Fe-Mg minerals in peraluminous granitoid rocks from central Spain. Eur J Mineral. 6:691–710

Whalen JB, Chappell BW (1988) Opaque mineralogy and mafic mineral chemistry of 1- and S-type granites of the Lachlan Fold belt, southeast Australia. Am Mineral. 73:281–296

Wiedenbeck M, Allé P, Corfu F, Griffin WL, Meier M, Oberli F, von Quadt A, Roddick JC, Spiegel W (1995) Three natural zircon standards for U-Th-Pb, Lu-Hf, trace element and REE analyses. Geostandards Newsletter. 19:1–23

Williams IS, Buick IS, Cartwright I (1996) An extended episode of early Mesoproterozoic metamorphic fluid flow in the Reynolds Range, central Australia. J Metamorph Geol. 14:29–48

Wolf M, London D (1997) Boron in granitic magmas: stability of tourmaline in equilibrium with biotite and cordierite. Contrib Mineral Petrol. 130:12–30

Wones DR, Eugster HP (1965) Stability of biotite: experiment, theory and application. Am Mineral. 50:1228–1272

Wyllie PJ, Sekine T (1982) The formation of mantle phlogopite in subduction zone hybridization. Contrib Mineral Petrol. 79:375–380

Yavuz F (2003) Evaluating micas in petrologic and metallogenic aspect: part II—applications using the computer program Mica+. Comput Geosci. 29:1215–1228

Yavuz F, Karakaya N, Yildirim DK, Karakaya MC (2014) A Windows program for calculation and classification of touramline-supergroup (IMA-2011). Comput Geosci. 63:70–87

Yoder JR, Kushiro I (1969) Melting of a hydrous phase; phlogopite. Am J Sci. 257-A:558–582

Zirkler A, Johnson TE, White RW, Zack T (2012) Polymetamorphism in the mainland Lewisian complex, NW Scotland — phase equilibria and geochronological constraints from the Cnoc an t'Sidhean suite. J Metamorph Geol. 30:865–885